Was Australia a sink or source of CO_2 in 2015? Data assimilation using OCO-2 satellite measurements

Yohanna Villalobos[1,2], Peter J. Rayner[1,2,3], Jeremy D. Silver[1,4], Steven Thomas[1], Vanessa Haverd[5], Jürgen Knauer[5], Zoë M. Loh[6], Nicholas M. Deutscher[7], David W.T. Griffith[7], and David F. Pollard[8]

[1]School of Earth Sciences, University of Melbourne, Australia
[2]ARC Centre of Excellence for Climate Extremes, Sydney, Australia
[3]Climate & Energy College, University of Melbourne, Australia
[4]School of Mathematics and Statistics, University of Melbourne, Australia
[5]CSIRO Oceans and Atmosphere, Canberra, 2601, Australia
[6]CSIRO Oceans and Atmosphere, Aspendale, Victoria 3195, Australia
[7]School of Earth, Atmospheric and Life Sciences, University of Wollongong, Wollongong, Australia
[8]National Institute of Water and Atmospheric Research Ltd (NIWA), Lauder, New Zealand.

Correspondence: Yohanna Villalobos (yvillalobos@student.unimelb.edu.au)

Abstract.

In this study, we present the assimilation of data from the Orbiting Carbon Observatory-2 (OCO-2) to estimate the Australian CO_2 surface fluxes for the year 2015. We used a regional-scale atmospheric transport-dispersion model and a four-dimensional variational assimilation scheme. Our results suggest that Australia was a carbon sink of -0.3 ± 0.09 PgC y^{-1} compared to the prior estimate 0.09 ± 0.17 PgC y^{-1} (excluding fossil fuel emissions). Most of the uptake occurred over northern savannas, the Mediterranean ecotype in southern Australia and the sparsely vegetated ecotype in central Australia. Our results suggest that the majority of the carbon uptake over Mediterranean was associated with positive EVI anomalies (relative to 2000-2014). However, the stronger posterior carbon uptake estimated over savanna and sparsely vegetated ecosystem was due primarily to underestimation of the gross primary productivity by the land surface model (CABLE-BIOS3 model). To evaluate the accuracy of our posterior flux estimates, we compare our posterior CO_2 concentration simulations against the column-averaged carbon retrievals from the Total Carbon Column Observing Network (TCCON) and ground-based in-situ monitoring sites located around our Australia domain. In general, the performance of our posterior concentration compared well with TCCON observations, except when TCCON concentrations were dominated by ocean fluxes which were tightly constrained to their prior values. Comparisons with in-situ measurements also show encouraging results though with similar difficulties for coastal stations. For stations located far from the coast, the comparison with in situ data was more variable, suggesting difficulties to match the column-integrated and surface data by the inversion, most likely linked to model vertical transport.

1 Introduction

Australia's carbon budget has been investigated by several large scale global ecosystem models (Sitch et al., 2015, Carbon cycle model intercomparison project (TRENDY)) and by the Regional Carbon Cycle Assessment and Processes project (RECCAP)

20 (Haverd et al., 2013a). However, although they have contributed to a more refined knowledge of the Australian carbon cycle, the estimated fluxes still diverge significantly. In the latest RECCAP report (Haverd et al., 2015), the net biome production (NBP) estimate for the country was a net carbon source of $0.59 \pm 0.35 \, \mathrm{PgC \, y^{-1}}$ between 1990–2011. A large component of the uncertainty in this carbon budget was attributed to the estimate of net primary productivity (NPP) over grassland (Haverd et al., 2013b), with a large contribution to the land cover type they used to force their simulations (e.g. The Advanced Very High

25 Resolution Radiometer AVHRR (1990–2006) (Donohue et al., 2009) and The Moderate Resolution Imaging Spectroradiometer (MODIS) (2000–2011). Given this uncertainty, it is essential to bring any other observations we have to bear on the Australian carbon balance.

Data assimilation (also called atmospheric transport inversion) along with an increase of remotely-sensed concentrations of carbon dioxide CO_2 data have been revolutionary for quantifying land-ocean-atmosphere CO_2 flux exchange in the last decade.

30 Satellite data from the Greenhouse Gases Observing Satellite (GOSAT) (Yokota et al., 2009) launched in 2009 and the Orbiting Carbon Observatory-2 (OCO-2) (Eldering et al., 2017) launched in 2014 have been used by several studies (Basu et al., 2013; Chevallier et al., 2014; Deng et al., 2014; Maksyutov et al., 2013; Crowell et al., 2019) to infer carbon CO_2 sources and sinks at continental scales. Few regional studies have been performed and none over Australia while the global inversions show large differences for this region. For example, a study based on six satellite-based inversions using GOSAT (Chevallier et al., 2014,

35 Fig.1) shows that Australia was a carbon sink ($\sim$ -0.7 PgC yr^{-1}) for 2010. For the same year, Basu et al. (2013) inferred it to be a net carbon source ($\sim$ 0.4 PgC yr^{-1})[1].

The accuracy of flux inversions using global CO_2 transport models has been the subject of discussion due to errors related to modelled transport (Chevallier et al., 2014; Basu et al., 2018). Transport model error in global inversions often emerges because inversions run at horizontal resolutions of 1°– 5°. Increasing the model resolution (Law et al., 2004), potentially reduces the

40 representation errors found in global-scale models. Regional-scale inversions arose about a decade ago. They rely on mesoscale transport models (at 1° down to 10 km resolution), for example, Broquet et al. (2011) performed a regional-scale variational inversion of the European biogenic CO_2 fluxes at 50 km resolution. Another example of regional-scale inverse modelling is found in Villalobos et al. (2020), who performed the inversion at 81 km resolution over Australia. Finer resolution models have the potential to be more successful since they can offer a better representation of surface CO_2 fluxes and variability, as well as

45 a better simulation of the processes driving high-frequency variability of transport (Schuh et al., 2010).

Australia has recently been subject to attention from the global carbon cycle community (Poulter et al., 2014) due to a large terrestrial carbon sink anomaly recorded in 2011. In this study, Poulter et al. (2014) found an Australia flux anomaly of -0.66 relative for the period 2003-2012. Trudinger et al. (2016) also found a similar carbon anomaly for this period of 0.40–0.61 PgC y^{-1}. These studies suggest that Australia's ecosystems might act as strong sinks of CO_2 in the future during extreme wet

50 periods. However, Ma et al. (2016) found that this carbon uptake rapidly diminished, ($\sim$ 0.08 PgC y^{-1}) for the period 2011–2012, suggesting that semi-arid ecosystem can act as a carbon sink in the relatively short term compared to tropical forests. An

---

[1]In this paper we adopt the atmospheric convention where a negative flux indicates removal from the atmosphere (a sink), and a positive value indicates an addition to the atmosphere (source).

Atmospheric
Chemistry
and Physics
Discussions
Open Access

important unanswered question in carbon cycle research remains regarding the carbon sink strength of semi-arid ecosystems in non-wet years.

In this study, we present a regional inversion to infer CO_2 fluxes over Australia for 2015 based on the Community Multiscale Air Quality (CMAQ) model and OCO-2 satellite retrievals. In 2015, Australia was affected by the El Niño Southern Oscillation (ENSO), and although some parts of continent were impacted by rainfall deficiency, other regions such as northern and south-eastern Australia rainfall was above average (BoM, 2015).

This manuscript is structured into five sections. Section 2 describes the flux inversions system, and the datasets used. Section 3 presents the main results of the Australian carbon budget, as well as an analysis of the EVI and rainfall anomalies, and a comparison between our posterior CO_2 concentration against the Total Carbon Column Observing Network (TCCON) and in-situ measurements. In Section 4 we present a discussion of our results, as well as a comparison of our optimized fluxes against five different global inversions. In Section 5 we summarise our findings.

2 Methodology and data

To estimate the Australian CO_2 surface fluxes for 2015 we followed the same four-dimensional variational assimilation scheme described in Villalobos et al. (2020). In this section, we will present a brief description of the system, and an update of all changes we made to the data used for our inversion.

2.1 Bayesian Inverse system

Finding the optimal value (x^a) of the CO_2 flux estimates, involves identification of the best fits between both observations (y) and a prior (or background) estimate (x^b) of these fluxes (Ciais et al., 2010; Rayner et al., 2019). Using Bayes' theorem and under the hypothesis of unbiased Gaussian-distributed errors of x^b and y, the best estimate of x^a (maximum a posteriori) is equivalent to finding the minimum of the cost function $J(x)$ shown in Eq. 1. Notation in this study follows (Rayner et al., 2019).

$$J(x) = \frac{1}{2} \left[(x - x^b)^T \mathbf{B}^{-1} (x - x^b) \right] + \frac{1}{2} \left[(\mathbf{H}(x) - y)^T \mathbf{R}^{-1} (\mathbf{H}(x) - y) \right] \qquad (1)$$

In Eq. 1, $\mathbf{H}$, represents the application of the forward model and the "observation operator", which allows us to map the model variables (e.g. fluxes) to observations. $\mathbf{R}$ represents the error covariance matrix of y, including the transport model error. $\mathbf{R}$ is defined as a diagonal matrix (details Section 2.5). x represents the control vector of unknowns. x includes not only CO_2 surface fluxes, but also initial and boundary conditions (details Section 2.2). $\mathbf{B}$ is the associated error covariance matrix of x_b, boundary and initial concentrations, and includes off-diagonal terms. In these off-diagonal values, we only include spatial and non-temporal correlations of the prior fluxes (details of the structure of the prior error covariance matrix is found in Section 2.4 in Villalobos et al. (2020)).

We calculate the minimum of $J(\boldsymbol{x})$ by an iterative process, and not by an analytical expression. This numerical problem requires the value of the cost function gradient $\nabla_{\mathbf{x}} J(\mathbf{x})$.

$$\nabla_x J = \mathbf{B}^{-1}(\boldsymbol{x} - \boldsymbol{x}^b) + \mathbf{H}^T(\mathbf{R}^{-1}[\mathbf{H}(\boldsymbol{x}) - \boldsymbol{y})]) \tag{2}$$

We compute $\mathbf{H^T}$ using the adjoint of the CMAQ model (version 4.5.1; Hakami et al., 2007). We can see in Eq. 2 that
85 $\mathbf{H^T}$ is applied to the vector $\mathbf{R}^{-1}(\mathbf{H}(\boldsymbol{x}) - \boldsymbol{y})$, which is often called the "adjoint forcing", and represents the error-weighted differences between the forward model and the observed concentrations. Applying the adjoint model to the adjoint forcing, running backward in time from t_{i-1} to t_0, allows us to construct the gradient of the cost function, $\nabla_x J(\boldsymbol{x})$. The algorithm that our inverse system uses to optimize the $J(\boldsymbol{x})$ is the Limited-memory BFGS (L-BFGS-B), implemented in the `scipy` python module (Byrd et al., 1995). Figure 1 shows a simplified version of how our inversion system works to find the optimal values
90 of CO_2 surface fluxes.

The error statistics of $\boldsymbol{x^a}$ are embodied in the posterior error covariance matrix ($\mathbf{A}$). In this study, $\mathbf{A}$ was computed by a series of observing system simulation experiments (OSSEs) carried out by (Villalobos et al., 2020, section 2.4.). Appendix D, Fig. D1 shows the spatial distribution of the posterior monthly uncertainties calculated in Villalobos et al. (2020).
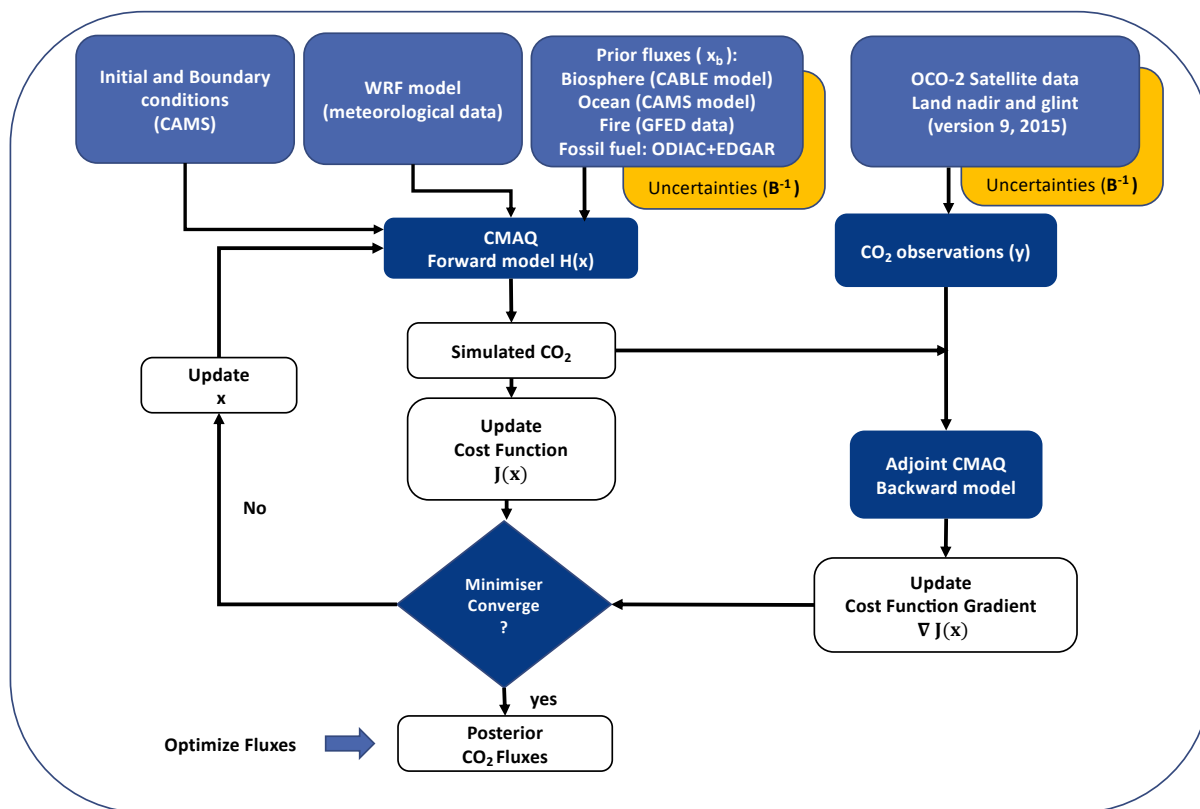

Figure 1. A simplified diagram of the four-dimensional variational data assimilation we used to estimate CO_2 surface fluxes over Australia.

2.2 Defining the Control Vector

95 Our control vector x, not only accounts for CO_2 surface fluxes, but also includes initial and boundary conditions. Prior estimates for these two variables were taken from the CAMS global CO_2 atmospheric inversion product (version v19r1) (Chevallier, 2019). We treated both the initial and boundary conditions as fixed patterns and solved for scaling factors. Uncertainties for the initial condition were set at 1% ($\approx$4 ppm). Lateral boundary conditions were added to eight boundary regions, where each boundary represents the upper and lower areas of the North, South, East and West sides of the CMAQ domain. These

100 values behave as offsets to a baseline boundary condition. The uncertainties in the lateral boundary conditions were assumed as the standard deviation (1σ uncertainty) of CAMS concentration data in the perimeter of the boundary. CMAQ can ingest 3-dimensional emissions so we treat the unknowns related to the boundaries as scaling factors for these emissions. We calculate their magnitudes from concentration tendencies in the CAMS data.

2.3 Prior information

105 We updated the prior CO_2 fluxes described in Villalobos et al. (2020, section 2.4). Biosphere carbon fluxes were derived using a modified version of the Community Atmosphere-Biosphere Land Exchange model (CABLE) (Haverd et al., 2018), which was forced by Australian regional drivers and observations (BIOS3 set-up). CABLE land surface model consists of a biophysical core: the Carnegie-Ames-Stanford Approach, Carbon, Nitrogen, Phosphorus (CASA-CNP) biogeochemical model (Wang et al., 2010), the POP module for woody demography and disturbance-mediated landscape heterogeneity (Haverd et al.,

110 2013c), and a module for land use and land management (POPLUC; Haverd et al. (2018)). For our regional study case, Harverd (2020) run CABLE model in BIOS-3 set-up (hereafter CABLE-BIOS3) at a resolution 0.25 degree. We calculated 3-Hourly biosphere CO_2 fluxes by combining two data sets: daily net ecosystem exchange (NEE) fluxes with 3-hourly Gross Primary Production (GPP). Given that the BIOS3 product did not cover our whole CMAQ model domain, we also incorporated monthly biosphere fluxes from Australia CABLE-POP global simulations. Australia CABLE-POP were run to be used in the Carbon

115 cycle model intercomparison project (TRENDY-v8) for the 2019 global carbon budget (Friedlingstein et al., 2019).

Anthropogenic fluxes were derived from two different inventory data sets: the Open-source Data Inventory for Anthropogenic CO_2 (ODIAC) (Oda et al., 2018) and the Emissions Database for Global Atmospheric Research (EDGAR) (Crippa et al., 2020). The combination of these two anthropogenic inventories (each used to cover different source sectors) was necessary because ODIAC did not contain emissions from aviation and marine transportation. We used the latest version of the

120 ODIAC emission data product, version 2019. ODIAC is a global gridded product distributed at $0.1° \times 0.1°$ spatial resolution over land using power plant profiles (emissions intensity and geographical location) and satellite-observed nighttime lights. We used ODIAC monthly fluxes and incorporated a diurnal scale factor to estimate diurnal CO_2 emission variability (Nassar et al., 2013). EDGAR is developed by the Netherlands Environmental Assessment Agency and the European Commission's Joint Research Centre. EDGAR is also gridded at $0.1° \times 0.1°$ with monthly temporal resolution.

125 We used monthly prior ocean fluxes from CAMS greenhouse gases flux inversion (version v19r1) (Chevallier, 2019). The prior fluxes that CAMS uses in its inversion also includes EDGAR emissions over the ocean; so we did not include this

anthropogenic flux over the ocean to avoid double counting. We also used monthly fire emissions from the Global Fire Emission Database, version 4 (GFED) (van der Werf et al., 2017), excluding small fire emissions. All these data were processed to hourly resolution and interpolated to the spatial resolution of the CMAQ model.

2.4 Atmospheric transport model

The inversion was based around the CMAQ modelling system (version, v5.3) and its adjoint (version 4.5.1; Hakami et al., 2007). The CMAQ modelling system is an Eulerian (gridded) mesoscale Chemical Transport Model (CTM). We added CO_2 into the CMAQ model as an inert chemical species, whose concentration is determined by atmospheric transport, fluxes, initial and boundary concentrations. The CMAQ model was driven by meteorological fields from the Weather Research and Forecast model (WRF) Advance Research Dynamical Core WRF-ARW (henceforth, WRF) version V4.1.1 (Skamarock et al., 2008), which data was processed by the Meteorology-Chemistry Interface Processor (MCIP) version 4.2 (Otte and Pleim, 2010). WRF configuration details are shown in Table 1. Our WRF model was set up at a spatial resolution of 81 km with 32 vertical layers from the surface up to 50 hPa. The numerical simulation was carried out on a single domain (i.e., non-nested). WRF initial conditions were taken from the ERA-Interim global atmospheric reanalysis (Dee et al., 2011), which has a resolution of approximately 80 km on 60 vertical levels from the surface up to 0.1 hPa. Sea surface temperatures were obtained from the National Centers for Environmental Prediction/Marine Modeling and Analysis Branch (NCEP/MMAB). The WRF model was run with a spin-up period of 12 hours.

Table 1. Physics parameterisations used in WRF model setup

Category	Selected schemes
Microphysics	Morrison double-moment (Morrison et al., 2009)
Short wave radiation	Rapid Radiative Transfer Model (RRTMG) scheme (Iacono et al., 2008)
Long-wave radiation	Rapid Radiative Transfer Model (RRTMG) scheme (Iacono et al., 2008)
Surface layer	Monin-Obukhov (Monin and Obukhov, 1954)
Land/water surface	The NOAH land-surface model and the urban canopy model (Tewari et al., 2007)
Planetary Boundary Layercs (PBL)	Mellor–Yamada–Janjic scheme (Janjić, 1994))
Cumulus	The Grell-Devenyi ensemble scheme (Grell and Dévényi, 2002)

2.5 OCO-2 satellite information

We assimilated satellite data from OCO-2 level 2 (Lite file version 9) for 2015, which is distributed by the National Aeronautics and Space Administration (NASA) (OCO-2 Science Team/Michael Gunson, Annmarie Eldering, 2018). OCO-2 provides nearly global coverage of column-averaged dry air mole fraction of CO_2 from space. Figure B1 in Appendix B shows the spatial distribution of OCO-2 soundings across the CMAQ domain for each month for 2015. We used bias-corrected data, as described by Kiel et al. (2019). We only selected land nadir and glint OCO-2 retrievals with a "good" quality flag. All OCO-2

soundings were averaged using a two-step process described in section 2.3 of Villalobos et al. (2020). The interpolation pro-
150 cedure between the OCO-2 retrieval grid and the CMAQ model vertical profile is described in section 2.6 of Villalobos et al.
(2020).

2.5.1 TCCON measurements

To validate our posterior CO_2 CMAQ concentrations, we used ground-based remote sensing data from the Total Carbon Col-
umn Observing Network (TCCON) (Wunch et al., 2011). There are three TCCON stations in our domain (see Table 2 for
155 references and Fig. 2 for coordinate locations). A TCCON instrument is a Fourier Transform Spectrometer (FTS) developed to
record direct solar spectra in the near-infrared spectral region. TCCON provides accurate and precise column-averaged concen-
trations of CO_2 and other greenhouse gases. This instrument represents the "gold standard" for surface-based remote-sensing
estimates of the total-column concentration of these gases. Data from TCCON is widely used by carbon cycle researchers,
in particular for global flux inversion and validation of satellite data products (such as from OCO-2). To perform a quantita-
160 tive comparison against CMAQ simulations, we averaged all the TCCON retrievals to create hourly average XCO2 values,
which were consistent with the CMAQ hourly simulations. After calculating the average of these retrievals, we interpolated
the TCCON column averaging kernels and TCCON a priori CO_2 profile to the CMAQ vertical profiles. After the interpolation,
we followed the equation (Eq.15 Connor et al., 2008) to compute the TCCON CMAQ simulated CO_2 concentrations. The
statistical analysis of CMAQ model–TCCON differences was based on monthly mean concentration, which were calculated
165 by taking daily mean averages (10:00 a.m. − 02:00 p.m.) local solar time, where the solar radiation intensity is most stable
(Kawasaki et al., 2012).

Table 2. Reference of the TCCON stations used in this work for evaluation of our inverse model system

TCCON station	Reference
Darwin, Australia	Griffith et al. (2014a)
Wollongong, Australia	Griffith et al. (2014b)
Lauder, New Zealand	Sherlock et al. (2014)

2.5.2 Ground-based in-situ measurements

Additional data sets used to validate our posterior concentrations were taken from four ground-based in-situ monitoring sites
forming part of the Global Atmosphere Watch (GAW) Programme of the World Meteorological Organisation (WMO): Cape
170 Grim, Gunn Point, Burncluith and Ironbark. Coordinates of these locations are shown in Fig. 2. All these data sets were supplied
by Loh (2019) at hourly temporal resolution. For the comparison with our model simulation, hourly data were converted to
monthly daily mean averages using only local solar time data (12:00 p.m - 05:00 p.m), where most of the OCO-2 soundings
were found.

Measurements of atmospheric CO_2 concentration at the Gunn Point, Ironbark and Burncluith sites were made continuously
at high frequency (~0.3 Hz) using CSIRO Picarro cavity ring-down spectrometers (model G2301 at Gunn Point and Ironbark,
and G2401 at Burncluith) all with inlets placed at the height of 10 m. Details of the Ironbark and Burncluith installation are
described by Etheridge et al. (2016), and are broadly similar to the installations elsewhere, including Gunn Point. Cape Grim
also operates a Picarro G2301 analyser, with the inlet positioned at a height of 70 m.

The instrumental precision for these analysers is better than $\pm$ 0.1 ppm for CO_2 (Etheridge et al., 2014) and all measure-
ments are calibrated to the WMO X2007 CO_2 mole fraction scale (Zhao and Tans, 2006), ensuring comparability between all
measurements used.

Cape Grim is a significant monitoring station in the GAW Programme because it samples air with some of the least recent
anthropogenic and terrestrial influence in the world, representing hemispheric background concentrations. These air masses,
known as "baseline", have blown straight off the Southern Ocean and have often been used in modelling studies. However,
in this study, we used all Cape Grim data because our inversion assimilates only data that comes from the land and carries
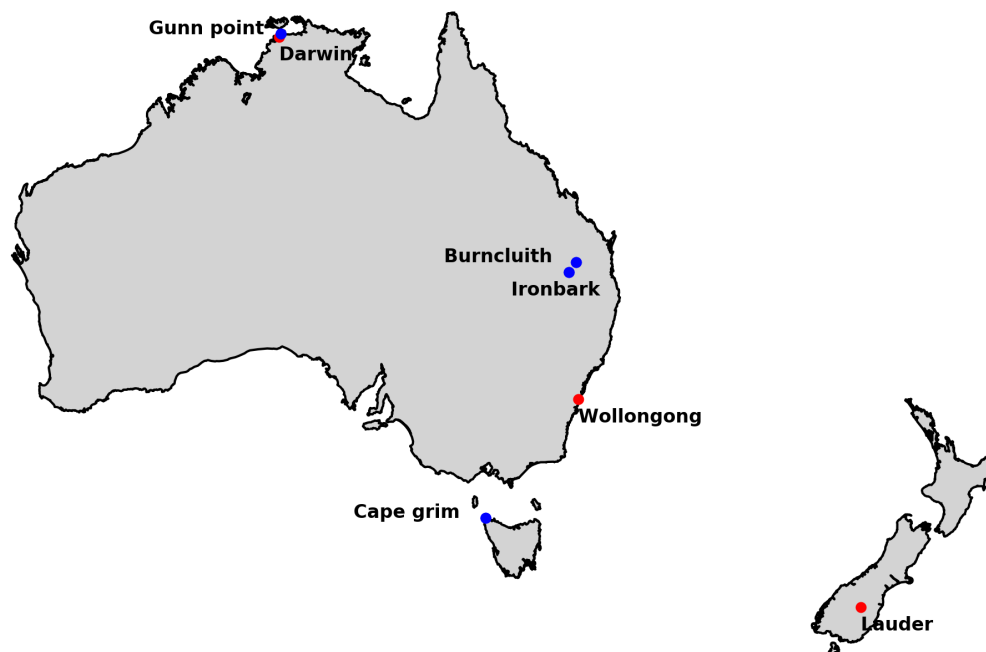terrestrial signals.

Figure 2. Total Carbon Column Observing Network (TCCON) and in-situ location sites. Red dots indicate TCCON locations. TCCON
Darwin and Wollongong are located over Australia, while TCCON Lauder is located in New Zealand. Blue dots represents in-situ location
around Australia (Gunn point, Burncluith, Ironbark and Cape Grim).

Atmospheric
Chemistry
and Physics
Discussions

2.6 Auxiliary data

In this study, we also assess auxiliary data such as the Enhanced Vegetation Index (EVI), rainfall, and gross primary productivity (GPP) from the BIOS-2 model to understand the difference between the prior and posterior fluxes over Australia in 2015.

2.6.1 The Enhanced Vegetation Index (EVI)

To understand if there was higher than expected growth of vegetation across Australia in 2015, we evaluated the monthly EVI anomalies relative to the long-term mean from 2000-2014. We used the EVI from the Moderate-Resolution Imaging Spectroradiometer (MODIS) MOD13C1 version 6 data product from the NASA satellite Terra (Didan, 2014). This gridded EVI MODIS product has a temporal resolution of 16 days composite and 0.05-degree spatial resolution. We constructed the EVI anomalies by subtracting the long-term mean (2000-2014) for each month of 2015. The spatial distribution of the EVI anomalies is shown in Supplementary Fig. S1. EVI measures the greenness of vegetation, and can be used as a proxy for monitoring the density or productivity of the vegetation biomass. EVI indices range from -0.2 to 1, where values less than 0 indicate a lack of green vegetation or arid areas. These monthly EVI MODIS products were regridded to the CMAQ grid to calculate the spatial correlation between prior and posterior flux differences (see Section 3.3).

2.6.2 Australian Water Availability Project (AWAP)

Monthly rainfall data was taken from the Australian Water Availability Project (AWAP), Bureau of Meteorology (BOM) (Jones et al., 2009). We used data for the period 2000–2015. AWAP data is obtained from a spline interpolation technique, which interpolates all available in situ rainfall observations onto grid-cells of 0.05 degrees (more details can be found in Jones et al., 2009). AWAP rainfall anomalies were calculated in the same way as EVI anomalies, by subtracting their long-term mean from 2000 to 2014 (see Supplementary Fig. S2).

2.6.3 MODIS Gross Primary Production (GPP)

We compared the MODIS Terra Gross Primary Productivity (GPP) MOD17A2H version 6 product for 2015 (Running et al., 2015) against BIOS model GPP predictions (see Appendix E, Fig. E1). The MODIS GPP product has a spatial resolution of 500 m and a temporal resolution of eight days. The 8-day composite was averaged to monthly resolution and aggregated to the CMAQ grid for comparison with the BIOS model GPP.

2.6.4 Global Atmospheric Inversions

We compared our posterior Australian biosphere CO_2 flux estimates (excluding fossil fuel) against five independent global atmospheric inversions (CAMS, CarbonTracker, Jena CarboScope versions (S76 and S85), MIROC4–ACTM; see Section 4). A summary of these five inversions is described in Table 3, and a complete description of them can be found in Le Quéré et al. (2018) (Appendix; Table A3). As we see in Table 3 all the global inversions were configured around different atmospheric

transport models and prior fluxes. Assumptions of the prior error covariance matrix and the type of in-situ measurements were also different.

Table 3. Summary of the inversion set-up and input fields of five different global inversions

Acronym	Reference	Grid spacing degrees	Transport Model	Number Vertical Layers	Prior Fluxes
CAMS	Chevallier et al. (2005)	$3.75° \times 1.875°$	LMDZ	39	ORCHIDEE
Jena CarboScope	Rödenbeck et al. (2003)	$4° \times 5°$	TM3	19	No prior
CarbonTracker	van der Laan-Luijkx et al. (2017)	$3° \times 2°$	TM5	25	SiBCASA–GFED4s
MIROC4	Patra et al. (2018)	$2.8° \times 2.8°$	ACTM	32	CASA

3 Results

3.1 Inversion Evaluation: Analysis of the residual between CMAQ simulation and OCO-2

220 As described in Eq. 1, the main purpose of the inversion is to optimize fluxes by minimizing the mismatch between the model simulation and observations. In order to evaluate the performance of the inversion, we compared the CO_2 concentrations obtained when forcing the CMAQ model with the prior and posterior fluxes (for convenience, we will call these the prior and posterior CO_2 concentrations, respectively). Fig. 3 shows the bias and root-mean-square error (RMSE) between the prior and posterior CMAQ simulations against the OCO-2 observations for 2015. This figure shows that the biases in the posterior

225 concentration were significantly reduced by the inversion. Our findings indicate that the prior concentrations overestimate OCO-2 from March to April, and from July to September. Prior biases in these months were reduced by more than 90%. In March, for example, the monthly mean bias was reduced from 0.59 to -0.02 ppm, with a decrease in the root mean square error (RMSE) from 1.19 to 0.89 ppm. On the other hand, in January, February, May and December prior biases were negligible, showing a good agreement with OCO-2. In a consistent system, we know that the theoretical value of the cost function at its

230 minimum should be close to half the number of assimilated observations, assuming all error statistics are correctly specified (Tarantola, 1987, p. 211). In our inversion, with 9,556 observations, the theoretical value we expected was 4,778. However, after more than 30 iterations we obtained a cost function of 10,071.11. This suggests that either prior uncertainties or observational uncertainties were too high (Rayner et al., 1999; Michalak et al., 2005). To compensate, the posterior uncertainties estimated in Villalobos et al. (2020) were increased by $\sqrt{2}$.
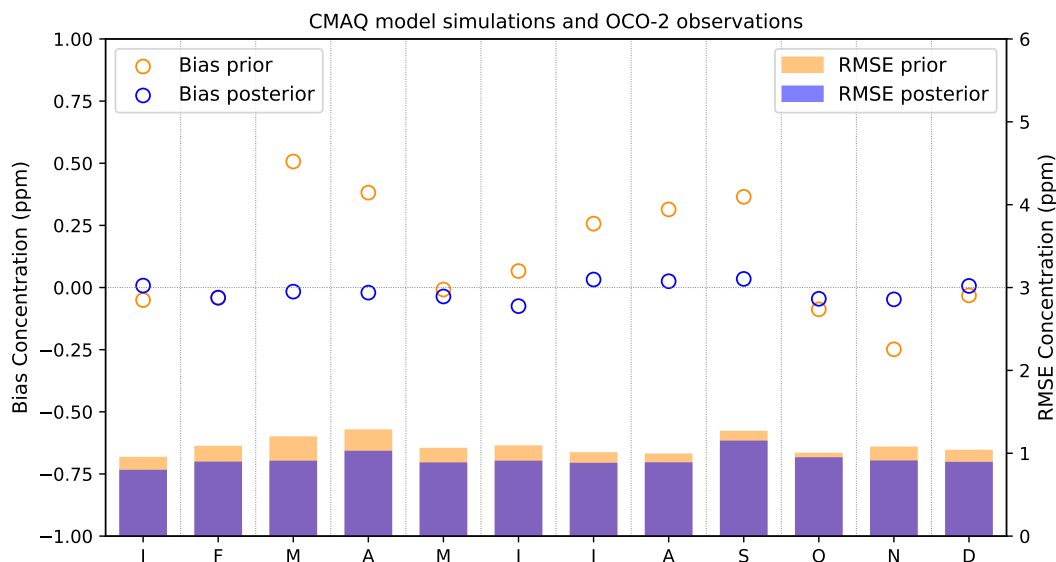
Figure 3. Bias and root mean square error (RMSE) between OCO-2 and the prior and posterior concentrations simulated by CMAQ model. Blue and orange circles represent prior posterior concentration biases, and orange and blue bars represent the RMSE.

3.2 Australian CO_2 flux estimate

Our results indicate that the Australian annual terrestrial flux (excluding fossil fuel) for 2015 was a slight carbon sink of -0.3 $\pm$ 0.09 PgC y^{-1} (1σ uncertainty) compared to the prior terrestrial estimate of 0.09 $\pm$ 0.17 PgC y^{-1}. Our prior fossil fuel estimates from ODIAC and EDGAR over Australia represent only 25% of the annual posterior flux, which is about 0.06 PgC y^{-1} (mostly constant for each month in 2015). We decided to exclude these emissions from our analysis because variations in land uptake cause most of the variation in our posterior fluxes. Figure 4a represents the terrestrial annual prior and posterior flux over Australia without fossil fuel emissions, while Fig. 4b shows monthly averages of these fluxes. Uncertainties included in both plots were calculated from an ensemble of five different OSSE experiments (for more details see Villalobos et al. (2020)) corrected by a factor of $\sqrt{2}$.

Fig. 4b shows that the posterior flux estimates generally refine the prior with exceptions in the second half of the year. In January and February the posterior fluxes were not modified much by the inversion. In January, for example, the terrestrial posterior flux was -0.65 $\pm$ 0.21 PgC y^{-1} compared to the prior -0.89 $\pm$ 0.63 PgC y^{-1}. The agreement follows from the small residual between prior simulated concentration and observation (Fig. 3). From March to May, we also see the posterior is shifted from the prior, although not significantly considering the prior uncertainty. In March, for instance, the prior flux (0.12 $\pm$ 0.62 PgC y^{-1}) was slightly shifted to a posterior carbon sink (-0.51 $\pm$ 0.20 PgC y^{-1}). However, these two estimates do not disagree because they fall within 1σ uncertainties.

July is one exception to this general agreement with a posterior flux of -1.71 $\pm$ 0.39 PgC y^{-1} compared to the prior flux of 0.09 $\pm$ 0.51 PgC y^{-1}. The spatial distribution of the posterior $-$ prior fluxes at grid-cell scale for July (Fig. A1, panel g) indi-

cates that the shift largely comes from northern and south-eastern Australia. The stronger posterior sink seen in July decreased

in August (-1.05 $\pm$ 0.31 PgC y^{-1}) and September (-0.61 $\pm$ 0.23 PgC y^{-1}), and changed sign in October and November. In

255 November, the posterior flux was 1.75 $\pm$ 0.31 PgC y^{-1} compared to the prior, which was 0.53 $\pm$ 0.58 PgC y^{-1}. The carbon

release from land in this period is likely attributed to fire activity from northern and south-eastern Australia (Appendix A,

Fig. A1, panel k). December is another interesting month because we see that the posterior source seen in November changed

again to a posterior sink of about -0.22 PgC y^{-1}. A further analysis which explains the reasons for this shift are shown in the
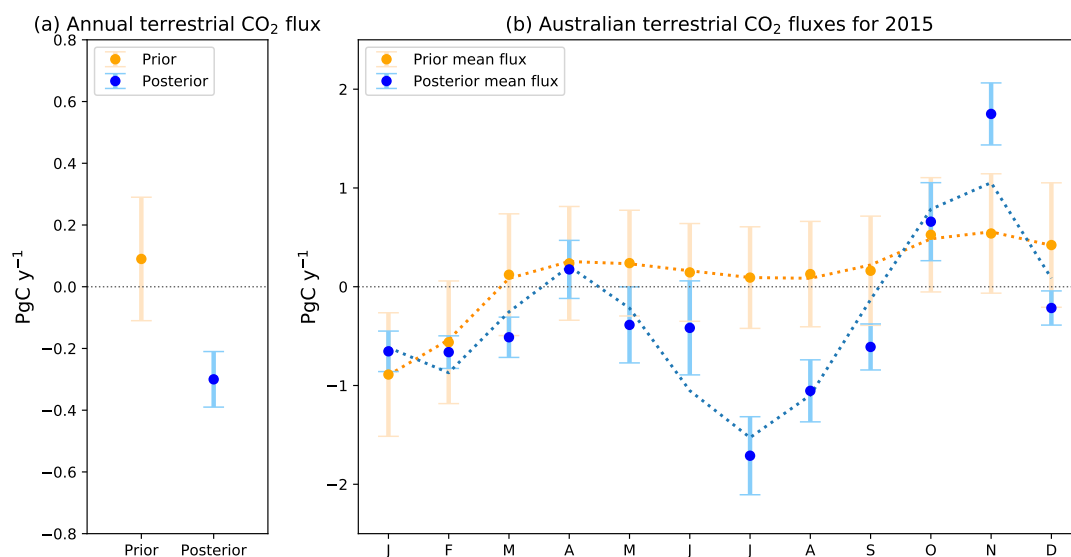
following section.

Figure 4. Time series of monthly mean prior (orange dots) and posterior (blue dots) CO$_2$ fluxes and their uncertainties in PgC y^{-1} over Australia for 2015. The orange and blue dashed line represents a smooth line for the prior and posterior fluxes respectively.

260   3.3   Spatial patterns of the EVI and rainfall anomalies in Australia

To investigate the increased uptake from July–September, we studied the spatial pattern of monthly EVI anomalies relative

to 2000$-$2014 over Australia from the MOD13C1 version 6 data product and rainfall anomalies from AWAP data relative

to 2000$-$2014 (Supplementary Figs. S1-S2). From the inversion viewpoint, the shift occurs because the prior simulation

overestimates OCO-2 concentration (see Fig. 3).

265   The spatial pattern of the difference between the posterior and prior estimate recorded in July indicates that the majority of

the posterior carbon uptake estimated by the inversion comes from the south-eastern and northern region of Australia (Appendix

B; Fig. B1, panel g). We found that the posterior sink estimated in south-eastern Australia was likely driven by a higher than

expected greenness of vegetation, probably induced by anomalously high rainfall in that period (Supplementary Fig. S1, panel

g). We cannot conclude the same related to the carbon uptake from the northern region. We can see in (Appendix A; Fig. A1,

270   panel g) that positive EVI anomalies in this area were not as strong as in south-eastern Australia. In the following section,

Atmospheric
Chemistry
and Physics
Discussions
Open Access
EGU

we will show that the underestimation of the GPP by the CABLE-BIOS3 model might be likely the reason for the difference between prior and posterior in this region. In August and September, we again see that most of the increased in the posterior flux comes from southern region of Australia (Supplementary Fig S1, panel g, h), which again lines up with a higher than usual increase in land productivity. Positive EVI anomalies in this period was not as strong as in July. These findings are in line with

275 the spatial pattern of the rainfall anomalies (Supplementary Fig S2, panel g, h). In August, the rainfall anomaly located in the south-western and south-eastern region decreased significantly, where only coastal areas received rainfall. In September, these rainfall anomalies dropped to negative in most parts of the country. Spatial patterns of the EVI anomalies during these months are expected because rainfall is one of the most important drivers of ecosystem dynamics and productivity. This is the case in (e.g. semi-arid) regions where rainfall is the limiting factor for plant growth, which is indeed the case in much of Australia.

280 These results are consistent with findings of previous studies (e.g., Weltzin et al., 2003) that Australia's semi-arid ecosystems are water resilient, and can respond to favourable rainfall conditions by capturing large amount of carbon.

3.4 Australian CO_2 flux estimate classified by bioclimatic zones

To understand which Australian ecosystem contributed most to our posterior carbon sink estimate, we divided the continent into six bioclimatic classes: tropical, savanna, warm temperate, cool temperate, Mediterranean and sparsely vegetated (Fig. 5).

285 We used the same six bioclimatic regions at a 0.05 degree spatial resolution as in Haverd et al. (2013a). The classes were regridded over our CMAQ grid (81×81 km) resolution. In this Figure, we can see that Australian tropical land only covers the northern coastal part of Australia. Savanna extends across the northern tropics to the south-eastern subtropical zone. Warm temperate land covers the south-east Australian coast, while cool temperate land covers the south-eastern corner of Australia. The Mediterranean region is confined to the south-western corner of Australia and the gulf region of South Australia. The

290 Sparsely vegetated ecosystem represents the biggest ecosystem over Australia, which extends from the northern subtropical zone to southern Australia.
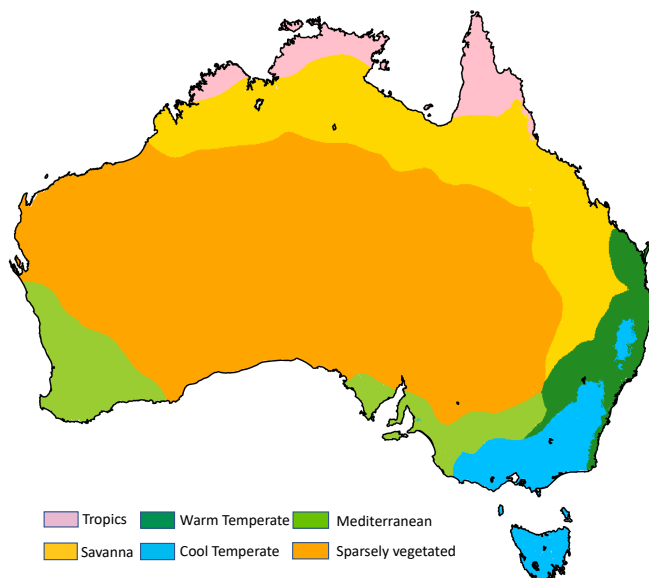
Figure 5. Bioclimatic classification of the Australian land cover.

The monthly time series of the prior and posterior terrestrial flux (not including fossil fuel) aggregated into these bioclimatic regions is shown in Fig. 6. We see that most of the prior and posterior sink estimated in January and February comes from savanna (Fig 6b). In February, in this ecosystem, we see that the prior sink (-0.55 $\pm$ 0.33 PgC y^{-1}) strengthens to a posterior (-1.05 $\pm$ 0.11 PgC y^{-1}). The anomalous sink coincides with the growing period (rainy season) for this region. Within Australian savanna lands, the major ecosystems are grasslands (Morgan et al., 2017). The vegetation growth in these lands respond favourably to rainfall.

Another noticeable difference between prior and posterior flux estimate over savanna is seen in July and August. In July, we cannot conclude if the prior was a sink or source of carbon (0.19 $\pm$ 0.28 PgC y^{-1}). However, our inversion indicates that Australia was acting as a carbon sink (-0.35 $\pm$ 0.11 PgC y^{-1}). In August, the prior source (0.25 $\pm$ 0.20 PgC y^{-1}) becomes a posterior carbon sink (-0.22 $\pm$ 0.08 PgC y^{-1}). To understand the difference between the prior and posterior estimate in this period, we calculated the GPP estimated by the CABLE BIOS-3 model and the GPP generated by MODIS (see Appendix E; Fig. E1, panel b). The temporal correlation between CABLE-BIOS3 and MODIS GPP was moderate (R = 0.69). According to MODIS estimates, the CABLE-BIOS3 GPP is overestimated from January to March, and underestimated from May to October. The underestimation of the GPP by the CABLE-BIOS3 model might explain why we find a stronger posterior sink estimated by our inversion in this category.

Over the warm temperate region, from February to April our posterior estimate suggests a source carbon (Fig 6c). For this period, we cannot determine if the prior flux estimate was a carbon sink or source due to its uncertainty range. In February, the prior flux (-0.05 $\pm$ 0.08 PgC) y^{-1} becomes a posterior carbon source (0.17 $\pm$ 0.06 PgC y^{-1}). In March, the prior estimate was nearly neutral (0.04 $\pm$ 0.05 PgC y^{-1}) compared to the posterior carbon source estimate (0.17 $\pm$ 0.05 PgC y^{-1}). The relative

small shift from the prior in this period was most likely because the CABLE-BIOS3 GPP over-estimates MODIS GPP (Fig. E1, panel c). For the warm temperate category, the correlation of BIOS and MODIS GPP is moderate (R = 0.86).

We also see a noticeable disagreement between prior and posterior estimates over the cool temperate ecosystem in April and May (Fig 6d). In this period, our posterior estimate indicates that this category was a stronger carbon source than the

315 prior flux estimate. In April, the inversion strengthened the prior source (0.12 ± 0.1 PgC y^{-1}) to a posterior (0.47 ± 0.05 PgC y^{-1}). In May, we cannot define if the prior was a sink or a source (0.06 ± 0.09 PgC y^{-1}), however, our assimilated fluxes indicate this category was acting as a posterior carbon source (0.36 ± 0.04 PgC y^{-1}). The analysis of GPP between the CABLE-BIOS3 model and MODIS also shows some discrepancies (see Appendix E; Fig. E1, panel d). For this category, in general, the CABLE-BIOS3 GPP is overestimating the productivity of the land for the whole year. For example, the absolute

320 difference between both GPP data set in April and June is about 0.2 PgC y^{-1}. For the Cool Temperate category the correlation between CABLE-BIOS3 and MODIS GPP is moderate (R = 0.73).

Another disagreement between the prior and posterior terrestrial flux estimate is seen over the Mediterranean ecoregion in August (Fig 6e). Our posterior estimate is a flux of -0.44 ± 0.09 PgC y^{-1} compared to the prior of -0.12 ± 0.10 PgC y^{-1}. The small reduction in uncertainty suggests caution interpreting this change. For this period, CABLE-BIOS3 underestimates

325 MODIS GPP by 0.2 PgC y^{-1}. August rainfall was also anomalously high in this region.

We found a noteworthy discrepancy between the prior and posterior flux estimate over sparsely vegetated ecosystem from May to September (Fig 6f). In this period, in general, the absolute difference between the prior and posterior mean was around 0.4 PgC y^{-1}. The largest difference was found in July and September, which was about 0.6 PgC y^{-1}. In this category, we believe that the stronger posterior sink estimated by our inversion might be associated with a underestimation of the GPP by

330 CABLE-BIOS3. The absolute difference between the CABLE-BIOS3 GPP and MODIS GPP was almost the same between May and September, which range was about $0.8-1.1$ PgC y^{-1}. This underestimation in GPP suggest also a underestimation of the land productivity. In this same category the posterior sink estimated in September disappears in October. For this period, our posterior source estimate (0.12 ± 0.09 PgC y^{-1}) did not present much difference with the prior (0.18 ± 0.11 PgC y^{-1}). In November and December, our posterior source was strengthen by the inversion. In November, we estimated a carbon source

335 of 0.39 ± 0.09 PgC y^{-1} in comparison with the prior, which was 0.12 ± 0.13 PgC y^{-1}. The extra carbon release estimated by the inversion might likely be associated with the fires located in the west and central north west region of Australia. We found this evidence analysing the Fire Information for Resource Management System (FIRM) (FIRM, 2020).
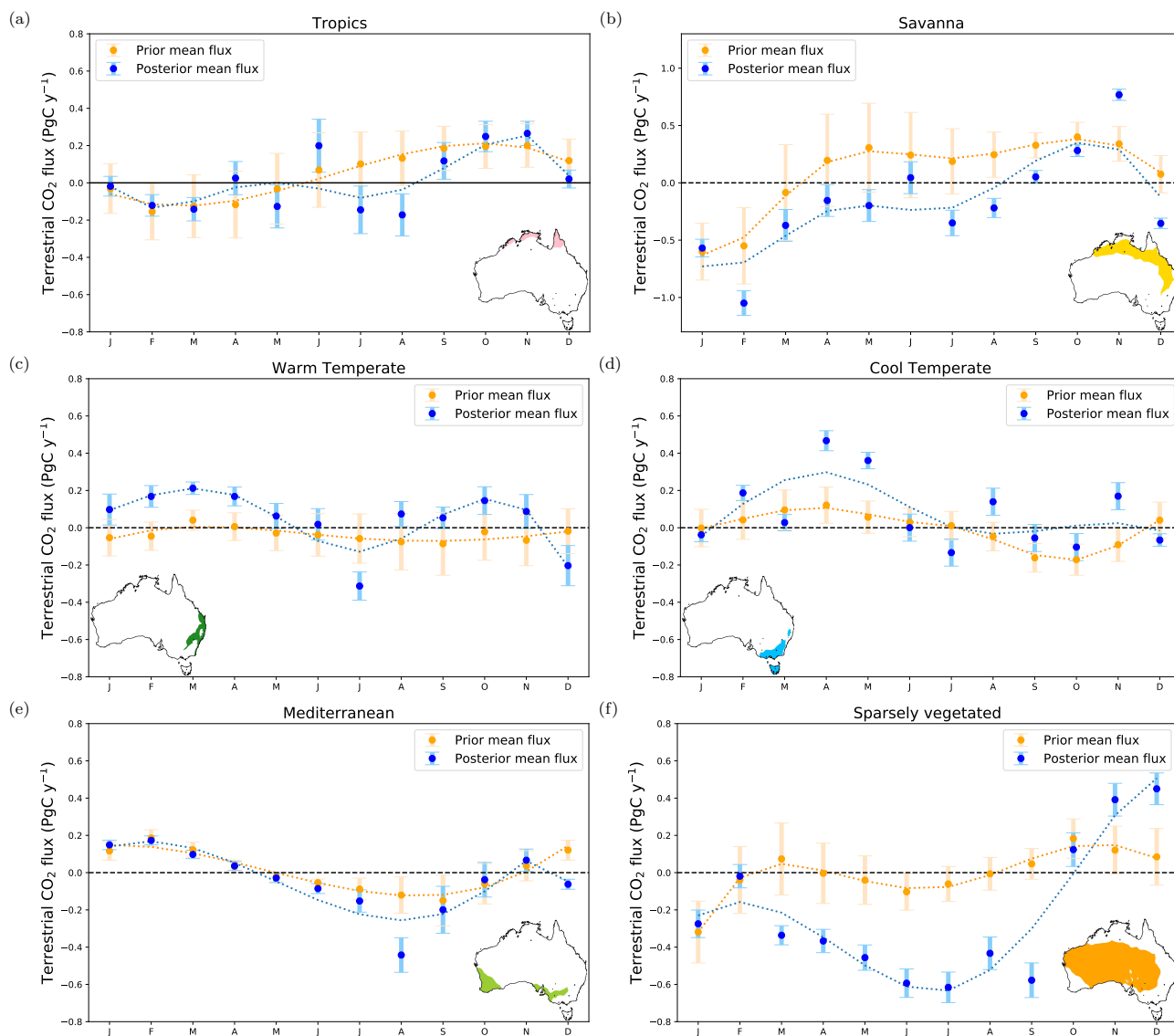
Figure 6. Monthly time series of the Australian land biosphere prior and posterior CO_2 flux and their uncertainties in PgC y^{-1} aggregated over six bioclimatic regions. The prior and posterior estimates do not include fossil fuel emissions.

3.5 Evaluation of the inversion with independent data

In this section we evaluate the accuracy of our posterior fluxes by comparing the prior and posterior CO_2 concentration simu-

340 lated by the CMAQ model against TCCON and in-situ observations.

3.5.1 Comparison with TCCON observations

As mentioned in section 2.5.1, we selected TCCON CO_2 observations from three different sites (Darwin, Wollongong and Lauder; see Fig. 2). The comparison between TCCON and the prior and posterior CO_2 concentrations, including both bias and root mean square error (RMSE) are shown in Figs. 7 and 8 respectively.

345   Despite a slight overestimation of our posterior concentration at TCCON Darwin site, we can see that overall, the posterior monthly mean concentration was well simulated by the CMAQ model in most months (Fig. 7a) and most of the biases were less than 1. ppm (Fig. 8). In general we found that the mean of the posterior concentration was shifted from the prior concentration towards the mean of TCCON observations. From February to April, for example, the prior biases were significantly reduced (range values between $25-80\%$). We also found that our posterior concentration were also better correlated with TCCON in

350   comparison with the prior concentration (R values range between 0.5 and 0.95; Appendix A, Table A1). Reduction of the biases from July to November and from November to December were also significant. In November and December (summer season in Australia), prior biases were reduced by more than 95%. On the other hand, posterior biases in June and October were not improved by the inversion. In June (winter season in Australia), biases were about 1.12 ppm (RMSE = 1.15). The high bias in this period could be associated to fire carbon emissions. Fire emissions are harder to estimate, especially since they are injected

355   at different variable heights. We did not re-distribute fires at across the column in CMAQ domain. We included all of them at the surface. Fires in June heavily impact the northern part of the country (dry season).

We also see a small overestimation of the posterior concentration at TCCON Wollongong site. At this particular location improvement of the bias were not as good as the TCCON Darwin site. Reduction of the prior biases was only seen for four months in 2015. In February (summer season) we see a reduction of the biases of about 15%. In June and July (winter season)

360   reduction of the prior biases were only 6% and 24%. In November (spring season in Australia) is the only month that we see a considerable improvement of the biases. In this period prior negative biases of about -0.74 ppm (RMSE = 1.22) were reduced to -0.24 ppm (RMSE = 1.18). We found that the highest biases were in August (1.76 ppm). High bias in these months may be related to strong westerly winds coming from areas (supplementary, Fig. S4), where there are too few OCO-2 soundings to constrain fluxes around the TCCON location (see Appendix B, Fig. B1, panel h).

365   Similar to Darwin and Wollongong site, we found a slight overestimation of our posterior concentration at TCCON Lauder site. Posterior biases were improved in June, July, September and November. In June and July (winter season) the reduction of the biases were only 7% and 12% respectively. Improvement of the biases in November and September were better (15 and 30%). We also did not find much improvement in the correlation for these months (R values $0.35-0.81$; Appendix A, Table A3). The small improvement of the biases at this site is likely due to a combination of New Zealand's size and shape,

370   the prevailing wind direction and the fact that we do not allow much freedom for ocean fluxes. Higher resolution models and smaller correlation lengths (allowing more flexibility in spatial fluxes) would be required for good performance over New Zealand.
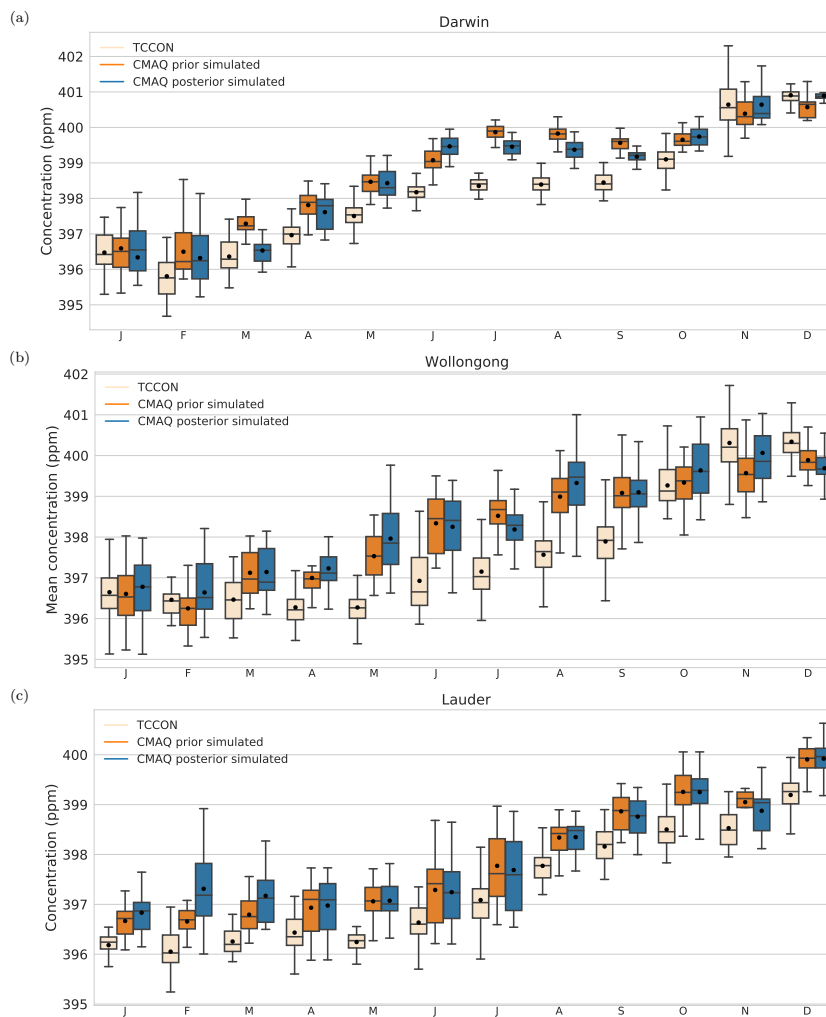
Figure 7. Box plot diagrams show the monthly mean average of CO_2 concentration at Darwin (a), Lauder (b) and Wollongong (c) TCCON site for 2015. The top edge of the box represents the 75th percentile and the bottom edge represents the 25th percentile. The top and bottom whiskers represent the 95th and the 5th percentile. The horizontal black line shows the median and the circle indicates the mean. Mean values are indicated by blue circles and median values by black line.
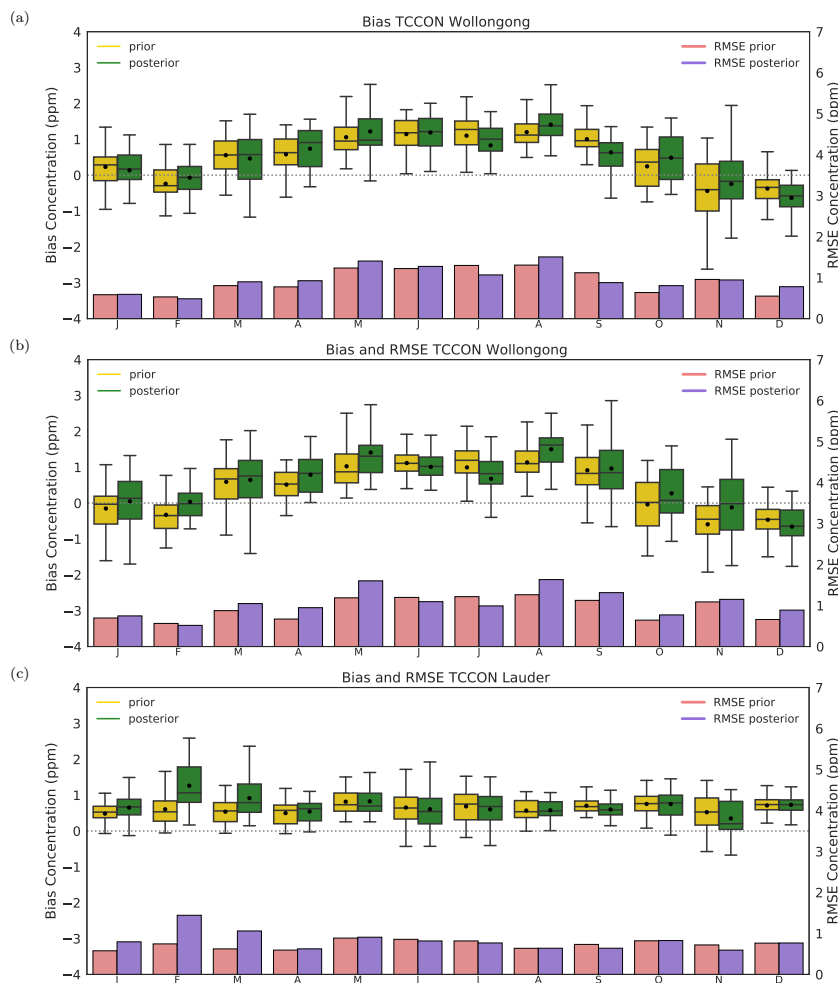
Figure 8. CMAQ prior and posterior concentration bias and root mean square error at TCCON sites (a) Darwin, (b) Wollongong and (c) Lauder for 2015. Yellow-green and green boxes represent prior posterior concentration biases and coral and purple bar represent the RMSE. Box plot represents the 75th percentile and the bottom edge represents the 25th percentile. The top and bottom whiskers represent the 95th and the 5th percentile. The horizontal black line shows the median and the circle indicates the mean. Mean values are indicated by black circles and median values by black line.

3.5.2   Comparison with in-situ measurements

We use four in situ measurement sites with sampling as described in Section 2.5.2. The comparison between prior and posterior
CO$_2$ concentration, as well as both bias and root mean square error (RMSE) are shown in Figs. 9 and 10 respectively.

As illustrated in Fig. 9a, the inversion does not match Gunn Point observed concentrations well except in February, September and November. Most biases are negative, indicating that the posterior simulation underestimates the observations. Negative biases in January and December can be related to strong westerly winds that blow from ocean onto land in this area (see

19

Atmospheric
Chemistry
and Physics

Discussions

Open Access

EGU

Supplementary; Fig. S6). Here, we must remember that we only used nadir and glint retrievals over land. Therefore the ocean

380 fluxes are scarcely optimised. The July error may well be related to a single event visible to the surface station but not to OCO2. On July 7th at 3:30 p.m Gunn Point registered a concentration of CO_2 of 558.40 ppm. It is probable that fires may have caused the high CO_2 concentration registered in this period (see information for July, 2015 at NASA Fire Information for Resource Management System (FIRM, 2020). This event was not captured by the inversion, causing a posterior concentration bias of -6.96 ppm.

385 We see good agreement between the posterior concentration and observations at Ironbark in January, April, May, September and November (Fig. 9b). We found high negative posterior biases in June and July. The negative posterior bias in June, -2.79 ppm (RMSE = 3.53), might be associated with the small number of OCO-2 soundings located around Ironbark (see Appendix C, panel f) and the wind direction in that region. We can see in Fig. S7 (Supplementary) that prevailing winds blow from the south-east, an area with no OCO-2 soundings to constrain fluxes. In July, posterior biases are larger than prior (-2.12 ppm to -

390 4.72 ppm). It is possible that the prior uncertainties that we introduced in the inversion were relatively high at Ironbark location, resulting in larger deviations from the prior and posterior flux, and subsequently in our posterior concentration location.

Results for the Burncluith station (Fig. 2c) are similar to Ironbark. This is not surprising given the stations' proximity. The posterior simulation performs better in July and October at Burncluith than Ironbark.

The posterior simulation at Cape Grim, shown in Fig. 9d, is in good agreement with the observations for the austral Autumn

395 and Winter of 2015. By contrast, high posterior biases are seen in September, November and December (> 2 ppm). This seasonality of bias is likely related to the seasonality of wind direction. the predominantly northerly flow in winter brings air from mainland Australia where fluxes have been constrained by OCO2 observations. The southerly flow later in the year brings air from the Southern Ocean, unconstrained by observations.
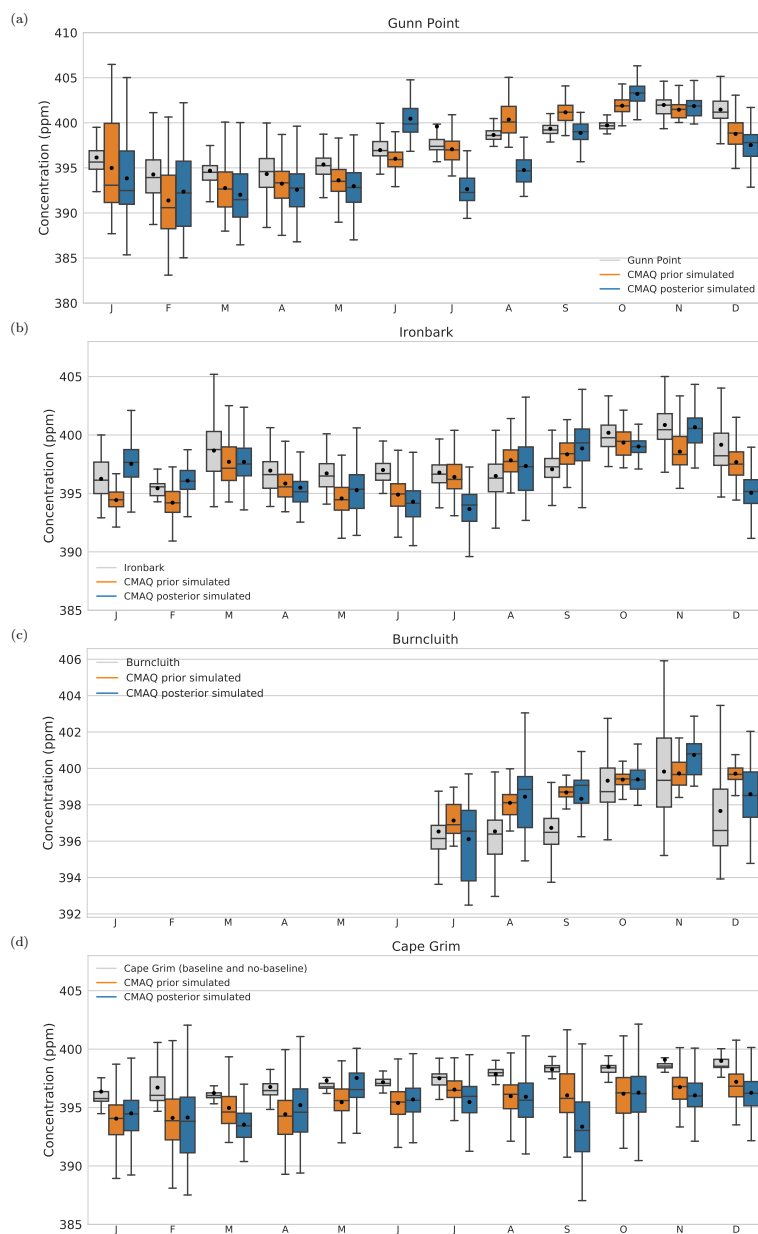
Figure 9. Box plot diagrams show the monthly mean average of CO_2 concentration at (a) Gunn point, (b) Ironbark, (c) Burncluith, and (d) Cape grim for 2015. For details of what the different components of the box-plot represent, see the caption of Fig. 7.

Figure 10. CMAQ prior and posterior concentration bias and root mean square error at (a) Gunn point, (b) Ironbark, (c) Burncluith, and (d) Cape grim for 2015. For details of what the different components of the box-plot repres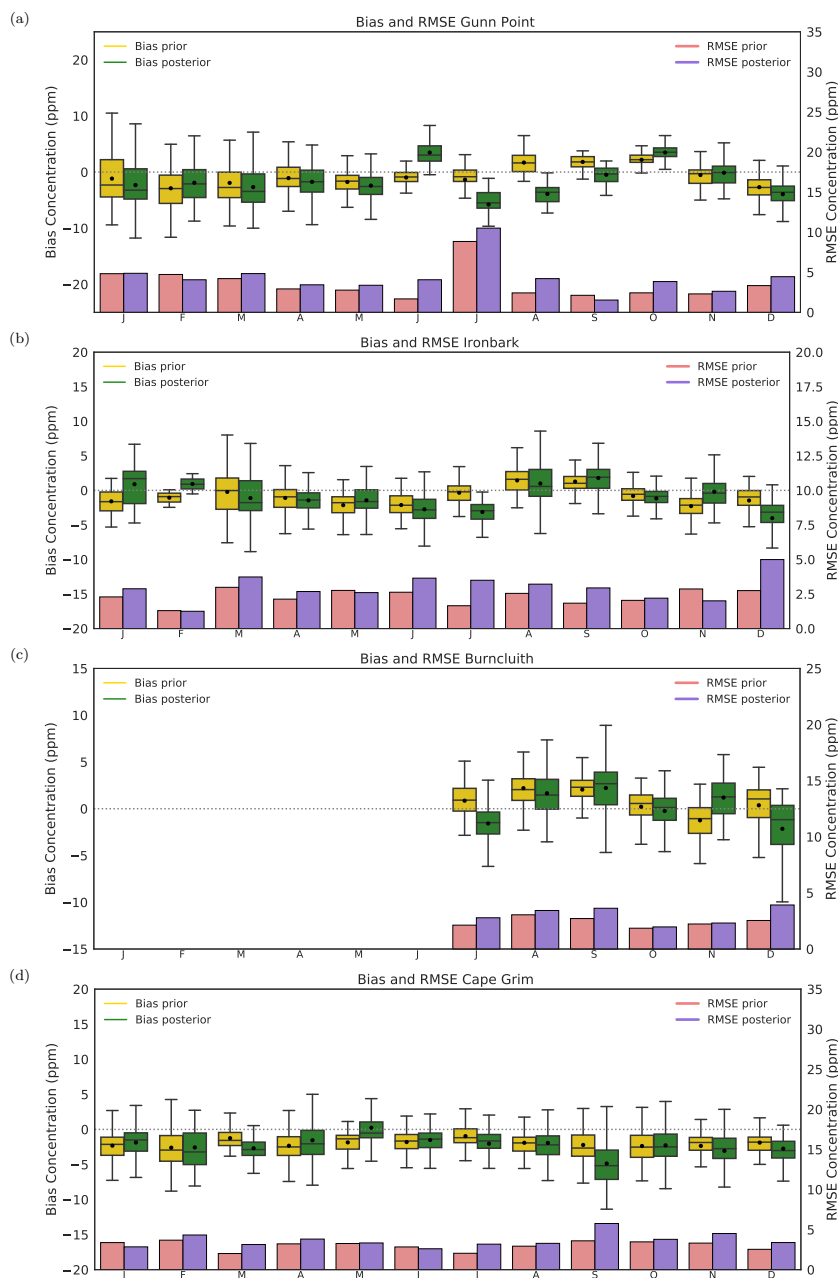ent, see the caption of Fig. 8. Note: Bias and RMSE in Gunn Point in July exclude the highest concentration value for that period, which was 558.408 ppm, we did this to better represent the Figure. Prior and posterior concentration bias for this period were -4.9 (RMSE = 16.8) and -5.1 ppm (RMSE = 17.1), respectively.

4 Discussion

400 We saw in section 4 that the most considerable difference between the prior and posterior carbon estimates was registered from July to September for 2015. Our inversion suggests a stronger carbon posterior sink compared to prior source in that period. We found that savanna, Mediterranean and sparsely vegetated ecosystem drove this higher posterior uptake. Positive EVI anomalies (relative to 2000−2014) suggests that this higher uptake of carbon in Mediterranean ecoregions was primarily driven by a higher than usual increase in vegetation productivity. Over sparsely vegetated ecoregion the higher carbon uptake

405 was mainly produced by an underestimation of the GPP by CABLE-BIOS3 land model. We speculate that the LAI estimated by the land-surface model CABLE-BIOS3 failed to capture the abrupt response of the terrestrial biosphere to rainfall. This hypothesis could be tested by comparing CABLE-BIOS3 LAI with satellite-LAI. This is beyond the scope of this study and will be taken up in a forthcoming article.

We compared our findings against an ensemble of five different global inversions: CAMS, CTRACKER, JENA-S76, JENA-

410 S85 and MIROC4–ACTM (see Table 3 for summary of the inversion set-up and Le Quéré et al. (2018) for complete details of them). The ensemble annual mean estimate of these global inversions for 2015 was 0.63 ± 1.15 PgC y^{-1} (Fig. 11a), compared to our posterior estimate (-0.30 ± 0.09 PgC y^{-1}). The ensemble spread is driven by model uncertainty which is not directly included in our posterior uncertainty estimate. It suggests our posterior uncertainty would be significantly larger if we could account for model uncertainty. Our inversion also produces a larger seasonal amplitude (3.46 PgC y^{-1}) than the ensemble

415 mean of the five global inversions (0.22 PgC y^{-1}) and CABLE-BIOS3 simulation (1.43 PgC y^{-1}). Table 4 shows a summary of this information and shows the peak-to-peak amplitude for each global inversion.

Table 4. Summary of the peak-to-peak amplitude of our posterior terrestrial fluxes, prior fluxes, and terrestrial fluxes from five different global inversions. Units PgC y^{-1}

Biosphere terrestrial fluxes	Acronym	Amplitude	Maximum month	Minumun month
	CAMS	0.27	September	February
	CTRACKER	0.15	December	March
Global inversions	JENA-S76	0.25	November	February
	JENA-S85	0.19	November	February
	MIROC4–ACTM	0.23	December	September
Prior	BIOS-CABLE3	1.43	November	January
Posterior	Fluxes assimilated by OCO-2	3.46	November	July

These global inversions are constrained only by in situ data which provide a weak constraint over Australia. In addition, these inversions use prior estimates produced by biosphere models such as CASA (van der Werf et al., 2017) or ORCHIDEE (Krinner et al., 2005). These models do not simulate well the NPP for grasslands (Wang et al., 2016) and hence underestimate

420 the seasonality of NEE for this important ecotype. This last point is critical for flux estimates over Australia because most of

the land ecosystem is grassland and shrubs. We conclude that OCO-2 data suggests a larger seasonal amplitude over Australia than most terrestrial biosphere models.

Monthly biases of simulated concentrations compared to TCCON sites at Darwin, Wollongong and Lauder generally improved using posterior rather than prior fluxes. This suggests that OCO-2, TCCON and the CMAQ model can produce a
425 mutually consistent description of Australian fluxes. Similar to the results found for the TCCON data, the posterior mean CO_2 concentrations simulated by CMAQ were also in good agreement with the in-situ observations, mainly at Cape Grim and Ironbark. The remaining negative posterior biases at Cape Grim are likely due to prevailing winds from the Southern Ocean, advecting air from regions unconstrained by OCO-2 data.
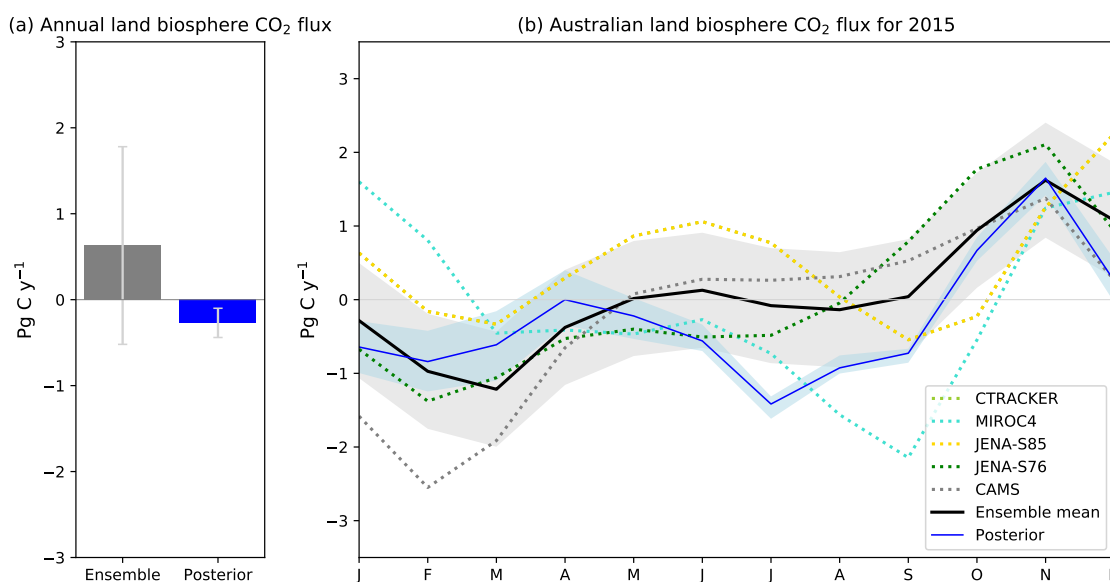

Figure 11. The grey bar plot in (a) shows the ensemble annual mean of five different global inversion(CAMS, CTRACKER, JENA-S76, JENA-S85 and MIROC4–ACTM for 2015. The error bar in this graph shows the spread of these models. The blue bar shows the annual mean posterior biosphere land CO_2 flux associated with its uncertainties (Note that the posterior uncertainties in this study were calculated by OSSEs). The black line in (b) shows the ensemble monthly mean of the five global inversions described in (a). The shaded area represents the $\pm \sigma$ uncertainty from the ensemble monthly the mean. The blue line represents the posterior flux estimated in this study (All fluxes in this comparison are without fossil fuel emissions).

The overall terrestrial carbon sink occurred despite the significant El Niño event (ECMWF, 2020). El Niño is only one of
430 several large-scale drivers of Australian climate and we have already noted positive rainfall anomalies associated with some strong sinks.

There are still several methodological choices that are somewhat arbitrary in this study. Most important is the implied spatial resolution. This is determined by the correlation length used in the prior uncertainty as much as the resolution of CMAQ. Villalobos et al. (2020) showed the impact of this correlation length on posterior uncertainty and our choice makes a

435 compromise between the information available from observations and avoidance of aggregation errors (Kaminski et al., 2001). A more important limitation is the restriction to one year. This will be addressed in a forthcoming study extending over the OCO-2 data set.

Higher-resolution flux inversions assimilating satellite retrievals of greenhouse gas concentrations, as illustrated by this study, will be increasingly important in a world seeking climate solutions and a better understanding of the global carbon cycle.
440 They will likely play a role not just addressing questions of scientific interest but also in ongoing monitoring and assessment of emission targets. Australia, as a large and geographically isolated land-mass, with a terrestrial biosphere highly responsive to climate drivers, offers an ideal testing ground for such flux inversions. The overall success of this study suggests great promise, especially in regions with sparse in situ networks.

5 Conclusions

445 We performed a four-dimensional variational data assimilation inversion to estimate Australian CO_2 fluxes for 2015. The inversion was based around the Community Multiscale Air Quality (CMAQ) transport-dispersion model, and satellite data from the Orbiting Carbon Observatory-2 (OCO-2) (land nadir and glint data, version 9). Our inverse estimates were tested against TCCON and in situ data. In general, they compared well with TCCON data when wind directions coupled our estimated fluxes to these observations. Comparison with in situ data was more variable, suggesting difficulties in simultaneously matching
450 column-integrated and surface data, most likely linked to model vertical transport. The posterior terrestrial biosphere flux estimate was -0.3 $\pm$ 0.09 PgC y^{-1} compared to the prior estimate of 0.09 $\pm$ 0.17 PgC y^{-1}. The savanna, Mediterranean and sparsely vegetated eco-regions were the primary driver for the posterior carbon sink observed mainly from July to September. Over the Mediterranean ecotype, we found that most of the carbon uptake was associated with positive EVI anomalies (relative to 2000-2014). However, the higher carbon uptake estimated over the savanna and sparsely vegetated ecosystem were mainly
455 due to an underestimation of GPP by CABLE-BIOS3. We also noted an increased seasonal cycle of flux, also suggesting greater productivity than the prior estimate.

Appendix A: Spatial pattern of the differences between posterior and prior fluxes
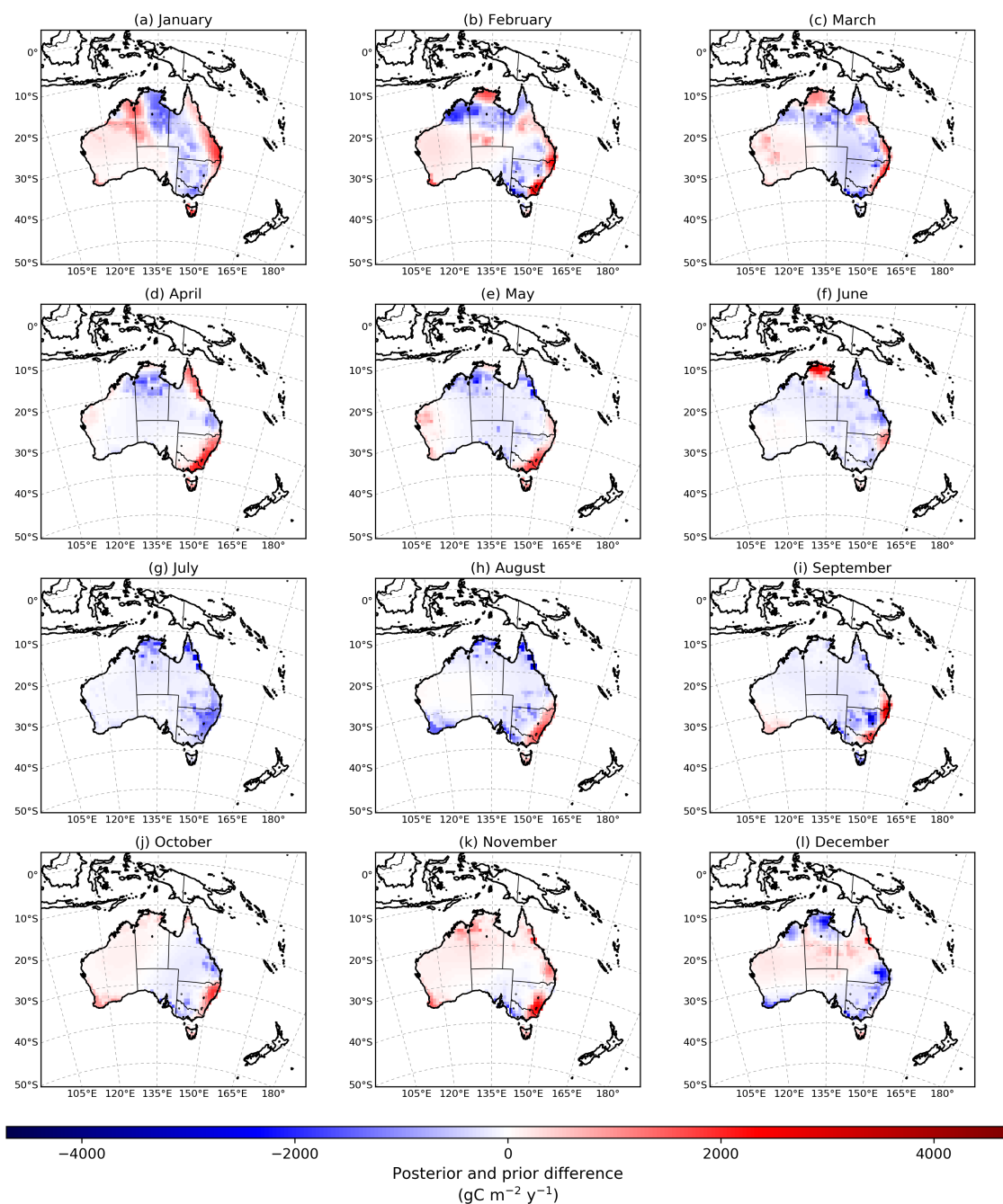

Figure A1. Spatial pattern of the differences between posterior and prior fluxes

Appendix B: Spatial distribution of OCO-2 data across Australia
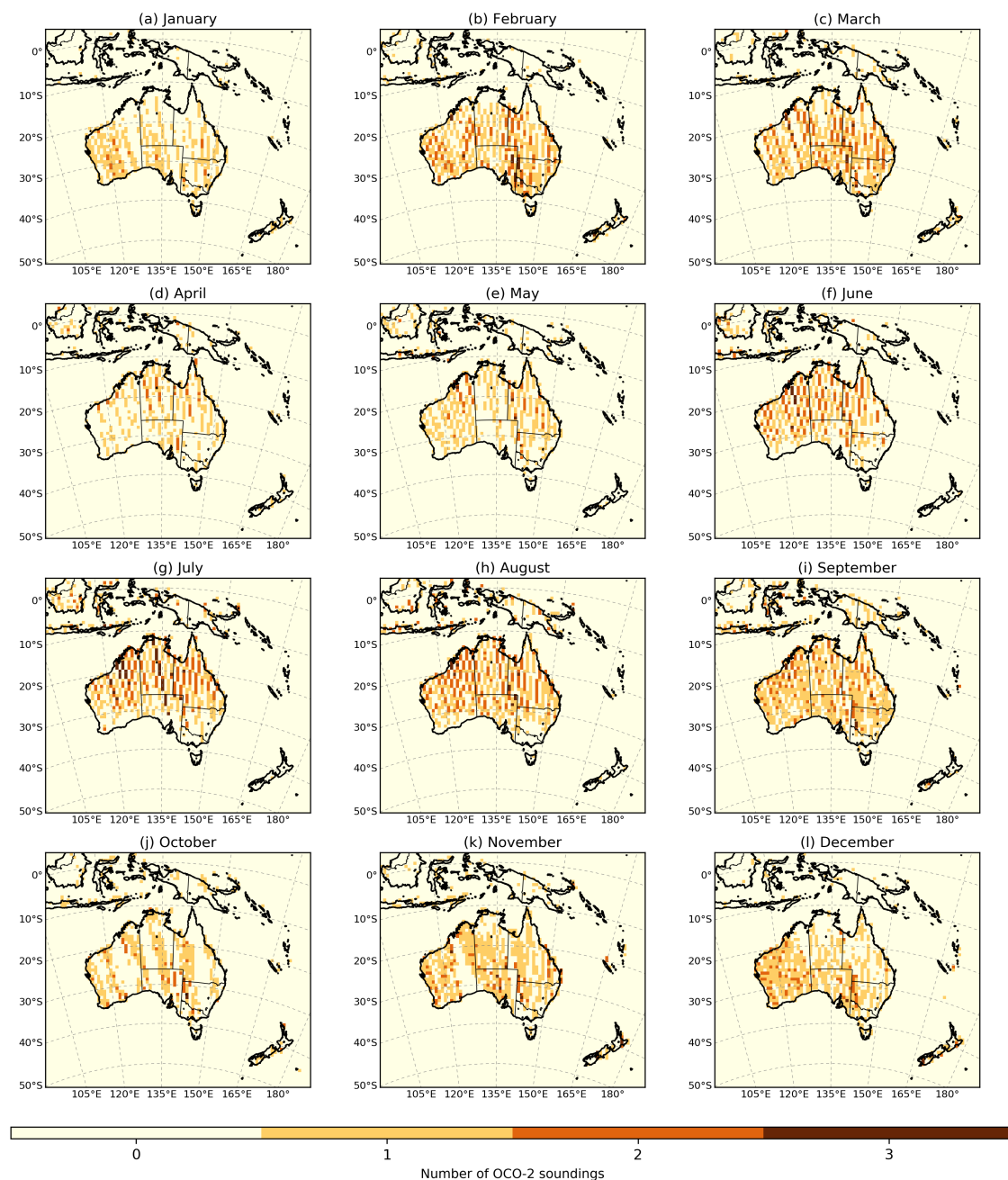
Figure B1. Spatial distribution of OCO-2 soundings (Land nadir and glint data) over the CMAQ domain for 2015.

Appendix C: Spatial distribution of the prior uncertainties across Australia
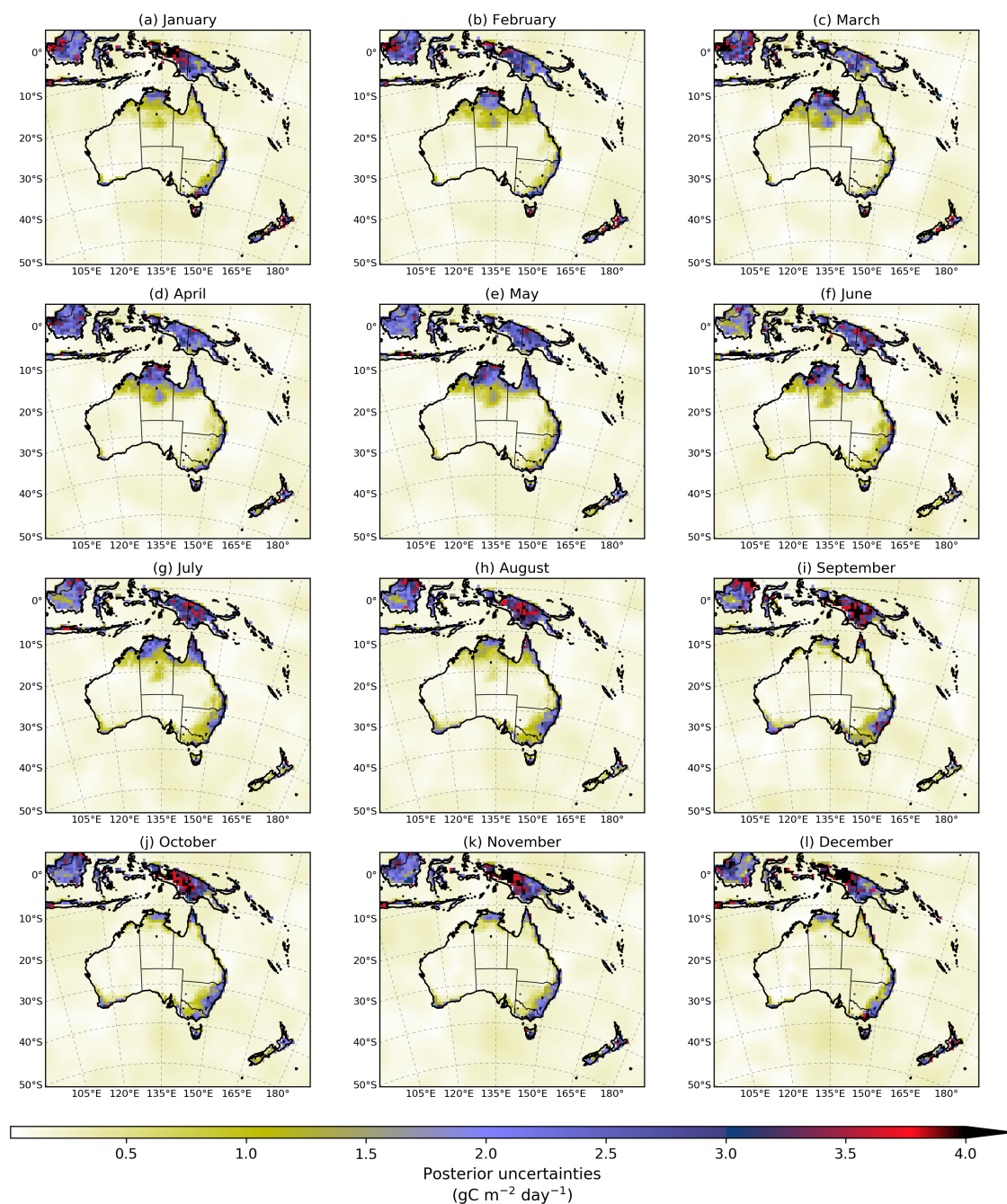
Figure C1. Prior uncertainties accounting for the major terms in the CO_2 budget (anthropogenic fluxes, fires, land and ocean exchange)

460 **Appendix D: Spatial distribution of the posterior uncertainties across Australia**

Figure D1. Posterior uncertainties calculated by OSSEs experiments in Villalobos et al. (2020)

Appendix E: Time series of BIOS GPP and MODIS GPP

Figure E1. Time series of monthly mean of CABLE-BIOS3 GPP and MODIS GPP
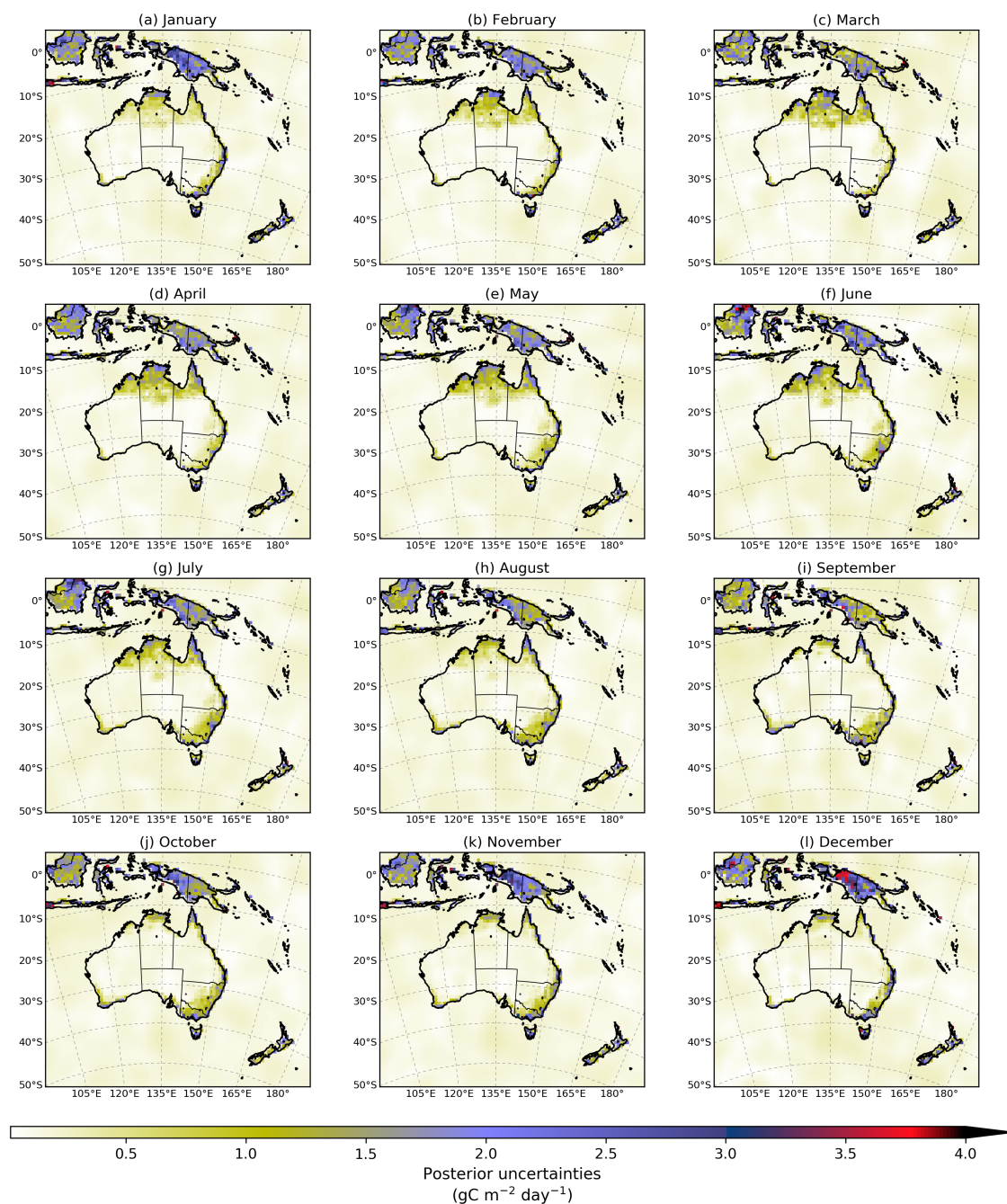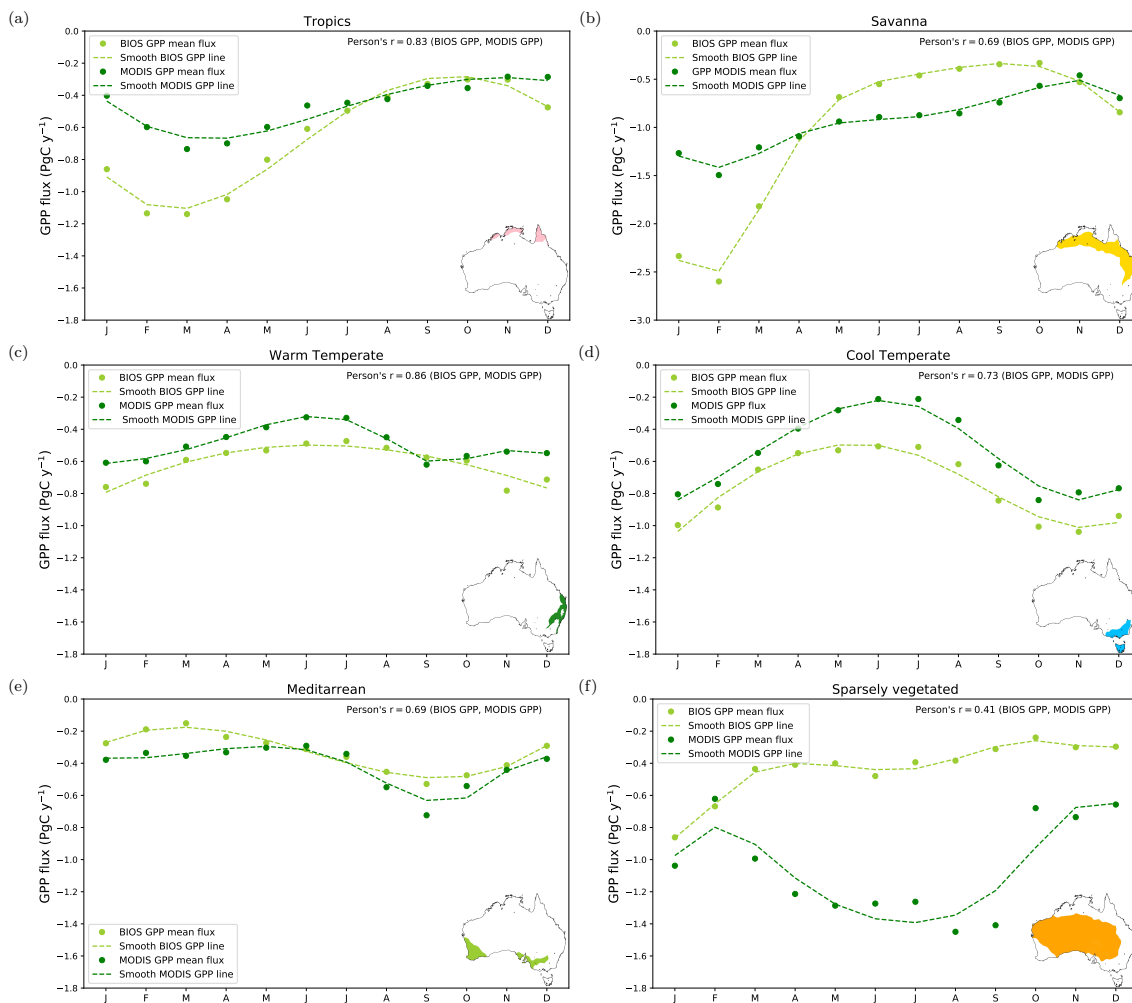
Atmospheric
Chemistry
and Physics
Discussions

Table A1. Analysis of the residual between CMAQ prior and posterior simulation and TCCON Darwin site for 2015. Averaged bias (Bias), Root-mean-square error (RMSE) and Pearson's coefficient (R).

	Darwin					
month	Prior			Posterior		
yyyy-mm-dd	Bias	RMSE	R	Bias	RMSE	R
2015-01-31	0.12	0.51	0.81	-0.14	0.87	0.87
2015-02-28	0.69	0.85	0.78	0.51	0.75	0.92
2015-03-31	0.93	1.10	0.14	0.17	0.60	0.50
2015-04-30	0.85	0.94	0.38	0.65	0.81	0.81
2015-05-31	0.97	1.05	0.37	0.93	1.02	0.76
2015-06-30	0.90	0.97	0.21	1.29	1.33	0.89
2015-07-31	1.51	1.55	-0.18	1.10	1.14	0.46
2015-08-31	1.44	1.46	0.34	0.98	1.03	0.66
2015-09-30	1.12	1.16	0.02	0.73	0.78	0.62
2015-10-31	0.55	0.63	0.53	0.64	0.70	0.89
2015-11-30	-0.25	0.51	0.66	0.00	0.41	0.91
2015-12-31	-0.34	0.48	0.18	-0.01	0.35	0.08

Table A2. Analysis of the residual between CMAQ prior and posterior simulation and TCCON Wollongong site for 2015. Averaged bias (Bias), Root-mean-square error (RMSE) and Pearson's coefficient (R).

| | Wollongong | | | | | |
| month | Prior | | | Posterior | | |
yyyy-mm-dd	Bias	RMSE	R	Bias	RMSE	R
2015-01-31	-0.04	0.72	0.21	0.14	0.79	0.22
2015-02-28	-0.21	0.56	0.48	0.18	0.70	0.41
2015-03-31	0.66	0.94	0.19	0.68	1.05	0.06
2015-04-30	0.72	0.96	0.07	0.96	1.20	0.20
2015-05-31	1.26	1.40	0.12	1.69	1.90	-0.04
2015-06-30	1.41	1.53	0.68	1.32	1.46	0.64
2015-07-31	1.37	1.56	0.32	1.03	1.29	0.26
2015-08-31	1.42	1.57	0.25	1.76	1.92	0.31
2015-09-30	1.19	1.44	0.16	1.21	1.54	0.16
2015-10-31	0.07	0.72	0.03	0.37	0.92	-0.02
2015-11-30	-0.74	1.22	-0.08	-0.24	1.18	-0.04
2015-12-31	-0.45	0.69	0.14	-0.65	0.94	-0.09

Table A3. Analysis of the residual between CMAQ prior and posterior simulation and TCCON Lauder site for 2015. Averaged bias (Bias), Root-mean-square error (RMSE) and Pearson's coefficient (R).

	Lauder					
month	Prior			Posterior		
yyyy-mm-dd	Bias	RMSE	R	Bias	RMSE	R
2015-01-31	0.48	0.58	0.31	0.65	0.80	0.09
2015-02-28	0.61	0.74	0.22	1.26	1.44	0.32
2015-03-31	0.54	0.62	0.51	0.92	1.06	0.52
2015-04-30	0.50	0.59	0.77	0.54	0.62	0.80
2015-05-31	0.82	0.89	0.30	0.83	0.91	0.18
2015-06-30	0.65	0.86	0.60	0.61	0.82	0.54
2015-07-31	0.69	0.82	0.79	0.60	0.77	0.76
2015-08-31	0.57	0.64	0.64	0.58	0.64	0.66
2015-09-30	0.71	0.73	0.83	0.60	0.64	0.82
2015-10-31	0.75	0.82	0.65	0.75	0.83	0.59
2015-11-30	0.52	0.72	0.36	0.35	0.59	0.35
2015-12-31	0.71	0.76	0.79	0.73	0.77	0.81

Table A4. Analysis of the residual between CMAQ prior and posterior simulation and Gunn Point site for 2015. Averaged bias (Bias), Root-mean-square error (RMSE) and Pearson's coefficient (R)

	Gunn Point					
month	Prior			Posterior		
yyyy-mm-dd	Bias	RMSE	R	Bias	RMSE	R
2015-01-31	-1.16	4.83	0.37	-2.31	4.87	0.27
2015-02-28	-2.88	4.73	0.41	-1.90	4.07	0.47
2015-03-31	-1.93	4.21	-0.06	-2.67	4.84	-0.03
2015-04-30	-1.07	2.92	0.33	-1.75	3.44	0.29
2015-05-31	-1.76	2.78	0.35	-2.41	3.38	0.51
2015-06-30	-0.96	1.68	0.29	3.49	4.07	0.31
2015-07-31	-2.53	16.46	0.00	-6.96	17.67	0.03
2015-08-31	1.70	2.43	0.41	-3.89	4.21	0.22
2015-09-30	1.81	2.13	0.28	-0.47	1.54	0.00
2015-10-31	2.19	2.44	0.15	3.49	3.84	-0.07
2015-11-30	-0.52	2.30	-0.67	-0.12	2.63	-0.74
2015-12-31	-2.69	3.34	0.38	-3.93	4.45	0.29

Table A5. Analysis of the residual between CMAQ prior and posterior simulation and Ironbark site for 2015. Averaged bias (Bias), Root-mean-square error (RMSE) and Pearson's coefficient (R)

	Ironbark					
month	Prior			Posterior		
yyyy-mm-dd	Bias	RMSE	R	Bias	RMSE	R
2015-01-31	-1.73	3.19	0.04	1.26	3.24	0.10
2015-02-28	-0.17	2.49	0.39	1.72	2.93	0.47
2015-03-31	2.96	3.78	0.43	2.94	4.12	0.10
2015-04-30	1.35	3.46	-0.24	0.96	3.50	-0.19
2015-05-31	-0.97	2.42	0.10	-0.27	2.26	0.22
2015-06-30	-2.19	2.83	0.18	-2.79	3.53	0.09
2015-07-31	-2.12	8.25	0.02	-4.72	9.54	-0.14
2015-08-31	-0.88	1.83	-0.05	-1.12	2.71	-0.02
2015-09-30	-1.00	1.81	-0.15	-0.34	2.43	0.04
2015-10-31	-0.39	1.43	-0.07	-0.76	1.41	0.06
2015-11-30	-2.53	2.82	0.63	-0.33	1.16	0.79
2015-12-31	-3.83	4.54	-0.09	-6.46	7.01	-0.05

Table A6. Analysis of the residual between CMAQ prior and posterior simulation and Burncluith site for 2015. Averaged bias (Bias), Root-mean-square error (RMSE) and Pearson's coefficient (R)

month	Prior			Posterior		
yyyy-mm-dd	Bias	RMSE	R	Bias	RMSE	R
2015-01-31	-	-	-	-	-	-
2015-02-28	-	-	-	-	-	-
2015-03-31	-	-	-	-	-	-
2015-04-30	-	-	-	-	-	-
2015-05-31	-	-	-	-	-	-
2015-06-30	-	-	-	-	-	-
2015-07-31	0.86	2.12	0.41	-1.57	2.77	0.28
2015-08-31	2.20	3.06	0.38	1.65	3.44	0.05
2015-09-30	2.03	2.69	0.44	2.20	3.61	0.20
2015-10-31	0.21	1.84	0.26	-0.24	1.96	0.13
2015-11-30	-1.24	2.23	0.73	1.19	2.31	0.68
2015-12-31	0.33	2.52	0.45	-2.18	3.93	0.06

(table header spanning: Burncluith)

Table A7. Analysis of the residual between CMAQ prior and posterior simulation and Cape Grim site for 2015. Averaged bias (Bias), Root-mean-square error (RMSE) and Pearson's coefficient (R)

		Cape Grim				
month		Prior			Posterior	
yyyy-mm-dd	Bias	RMSE	R	Bias	RMSE	R
2015-01-31	-2.31	3.38	0.28	-1.87	2.85	0.28
2015-02-28	-2.65	3.68	0.57	-2.58	4.29	0.46
2015-03-31	-1.25	2.02	0.53	-2.69	3.14	0.23
2015-04-30	-2.33	3.22	0.41	-1.55	3.82	0.15
2015-05-31	-1.85	3.27	0.36	0.23	3.34	0.42
2015-06-30	-1.77	2.79	0.14	-1.47	2.57	0.13
2015-07-31	-0.96	2.05	0.10	-2.03	3.19	-0.01
2015-08-31	-1.91	2.93	-0.05	-1.93	3.29	0.04
2015-09-30	-2.29	3.63	-0.02	-4.91	5.78	0.09
2015-10-31	-2.34	3.44	0.08	-2.23	3.76	-0.02
2015-11-30	-2.35	3.32	0.34	-3.06	4.51	-0.13
2015-12-31	-1.86	2.51	0.58	-2.76	3.38	0.37

Data availability. Data available on request from the authors

Code availability. The code of the inversion system is available at https://github.com/steven-thomas/py4dvar (Thomas, 2020).

Author contributions. YV prepared all the input data required to run the inversion system and performed data analysis of the fluxes. YV
465 was responsible for post-processing the TCCON and in-situ measurements, then developing the paper and figures. ST was the principal
developer of the inversion system code. PR and JR also contributed to developing the inversion code, provided guidance for the manuscript's
preparation and interpretation of the results. JK and VH ran CABLE-BIOS3 and provided the biosphere fluxes required for the inversion.
JK reviewed and commented on the final manuscript. ZL provided data from the ground-based in-situ measurements (Cape Grim, Ironbark,
Burncluith and Gunn Point) and gave comments on the paper. DP reviewed and comments on the TCCON Lauder site. ND and DG reviewed
470 the final manuscript.

Competing interests. The authors declare that they have no conflict of interest.

References

Basu, S., Guerlet, S., Butz, A., Houweling, S., Hasekamp, O., Aben, I., Krummel, P., Steele, P., Langenfelds, R., Torn, M., Biraud, S., Stephens, B., Andrews, A., and Worthy, D.: Global CO_2 fluxes estimated from GOSAT retrievals of total column CO_2, Atmospheric Chemistry and Physics, 13, 8695–8717, https://doi.org/10.5194/acp-13-8695-2013, http://www.atmos-chem-phys.net/13/8695/2013/, 2013.

Basu, S., Baker, D. F., Chevallier, F., Patra, P. K., Liu, J., and Miller, J. B.: The impact of transport model differences on CO_2 surface flux estimates from OCO-2 retrievals of column average CO_2, Atmospheric Chemistry and Physics, 18, 7189–7215, https://doi.org/10.5194/acp-18-7189-2018, https://www.atmos-chem-phys.net/18/7189/2018/, 2018.

BoM: Annual climate statement 2015, http://www.bom.gov.au/climate/annual_sum/2015/Annual-Climate-Report-2015-HR.pdf, 2015.

Broquet, G., Chevallier, F., Rayner, P., Aulagnier, C., Pison, I., Ramonet, M., Schmidt, M., Vermeulen, A. T., and Ciais, P.: A European summertime CO_2 biogenic flux inversion at mesoscale from continuous in situ mixing ratio measurements, 116, https://doi.org/10.1029/2011JD016202, https://agupubs.onlinelibrary.wiley.com/doi/abs/10.1029/2011JD016202, 2011.

Byrd, R., Lu, P., Nocedal, J., and Zhu, C.: A Limited Memory Algorithm for Bound Constrained Optimization, SIAM Journal on Scientific Computing, 16, 1190–1208, https://doi.org/10.1137/0916069, https://doi.org/10.1137/0916069, 1995.

Chevallier, F.: personal communication, 2019.

Chevallier, F., Engelen, R. J., and Peylin, P.: The contribution of AIRS data to the estimation of CO_2 sources and sinks, Geophysical Research Letters, 32, 1–4, https://doi.org/10.1029/2005GL024229, 2005.

Chevallier, F., Palmer, P. I., Feng, L., Boesch, H., O'Dell, C. W., and Bousquet, P.: Toward robust and consistent regional CO_2 flux estimates from in situ and spaceborne measurements of atmospheric CO_2, Geophysical Research Letters, 41, 1065–1070, https://doi.org/10.1002/2013GL058772, http://doi.wiley.com/10.1002/2013GL058772, 2014.

Ciais, P., Rayner, P., Chevallier, F., Bousquet, P., Logan, M., Peylin, P., and Ramonet, M.: Atmospheric inversions for estimating CO2 fluxes: methods and perspectives, Climatic Change, 103, 69–92, https://doi.org/10.1007/s10584-010-9909-3, http://link.springer.com/10.1007/s10584-010-9909-3, 2010.

Connor, B. J., Boesch, H., Toon, G., Sen, B., Miller, C., and Crisp, D.: Orbiting Carbon Observatory: Inverse method and prospective error analysis, Journal of Geophysical Research Atmospheres, 113, 1–14, https://doi.org/10.1029/2006JD008336, 2008.

Crippa, M., Solazzo, E., Huang, G., Guizzardi, D., Koffi, E., Muntean, M., Schieberle, C., Friedrich, R., and Janssens-Maenhout, G.: High resolution temporal profiles in the Emissions Database for Global Atmospheric Research, Scientific Data, 7, 121, https://doi.org/10.1038/s41597-020-0462-2, https://doi.org/10.1038/s41597-020-0462-2, 2020.

Crowell, S., Baker, D., Schuh, A., Basu, S., Jacobson, A. R., Chevallier, F., Liu, J., Deng, F., Feng, L., McKain, K., Chatterjee, A., Miller, J. B., Stephens, B. B., Eldering, A., Crisp, D., Schimel, D., Nassar, R., O'Dell, C. W., Oda, T., Sweeney, C., Palmer, P. I., and Jones, D. B. A.: The 2015–2016 carbon cycle as seen from OCO-2 and the global in situ network, Atmospheric Chemistry and Physics, 19, 9797–9831, https://doi.org/10.5194/acp-19-9797-2019, https://www.atmos-chem-phys.net/19/9797/2019/, 2019.

Dee, D. P., Uppala, S. M., Simmons, A. J., Berrisford, P., Poli, P., Kobayashi, S., Andrae, U., Balmaseda, M. A., Balsamo, G., Bauer, P., Bechtold, P., Beljaars, A. C. M., van de Berg, L., Bidlot, J., Bormann, N., Delsol, C., Dragani, R., Fuentes, M., Geer, A. J., Haimberger, L., Healy, S. B., Hersbach, H., Hólm, E. V., Isaksen, L., Kållberg, P., Köhler, M., Matricardi, M., McNally, A. P., Monge-Sanz, B. M., Morcrette, J.-J., Park, B.-K., Peubey, C., de Rosnay, P., Tavolato, C., Thépaut, J.-N., and Vitart, F.: The ERA-Interim reanalysis: configuration and performance of the data assimilation system, Quarterly Journal of the Royal Meteorological Society, 137, 553–597, https://doi.org/10.1002/qj.828, 2011.

515   Deng, F., Jones, D. B. A., Henze, D. K., Bousserez, N., Bowman, K. W., Fisher, J. B., Nassar, R., O'Dell, C., Wunch, D., Wennberg, P. O.,
        Kort, E. A., Wofsy, S. C., Blumenstock, T., Deutscher, N. M., Griffith, D. W. T., Hase, F., Heikkinen, P., Sherlock, V., Strong, K., Sussmann,
        R., and Warneke, T.: Inferring regional sources and sinks of atmospheric CO$_2$ from GOSAT XCO2 data, Atmospheric Chemistry and
        Physics, 14, 3703–3727, https://doi.org/10.5194/acp-14-3703-2014, http://www.atmos-chem-phys.net/14/3703/2014/, 2014.

      Didan, K.: MOD13C1 MODIS/Terra Vegetation Indices 16-Day L3 Global 0.05Deg CMG V006 [Data set], https://doi.org/10.5067/MODIS/
520   MOD13C1.006,lastaccessed2019-06-07, 2014.

      Donohue, R. J., McVICAR, T. R., and RODERICK, M. L.: Climate-related trends in Australian vegetation cover as inferred from satellite ob-
        servations, 1981-2006, Global Change Biology, 15, 1025–1039, https://doi.org/10.1111/j.1365-2486.2008.01746.x, https://onlinelibrary.
        wiley.com/doi/abs/10.1111/j.1365-2486.2008.01746.x, 2009.

      ECMWF: The 2015/2016 El Niño and beyond, https://www.ecmwf.int/en/newsletter/151/meteorology/2015-2016-el-nino-and-beyond,
525   2020.

      Eldering, A., O'Dell, C. W., Wennberg, P. O., Crisp, D., Gunson, M. R., Viatte, C., Avis, C., Braverman, A., Castano, R., Chang, A.,
        Chapsky, L., Cheng, C., Connor, B., Dang, L., Doran, G., Fisher, B., Frankenberg, C., Fu, D., Granat, R., Hobbs, J., Lee, R. A. M.,
        Mandrake, L., McDuffie, J., Miller, C. E., Myers, V., Natraj, V., O'Brien, D., Osterman, G. B., Oyafuso, F., Payne, V. H., Pollock, H. R.,
        Polonsky, I., Roehl, C. M., Rosenberg, R., Schwandner, F., Smyth, M., Tang, V., Taylor, T. E., To, C., Wunch, D., and Yoshimizu, J.:
530   The Orbiting Carbon Observatory-2: First 18 months of science data products, Atmospheric Measurement Techniques, 10, 549–563,
        https://doi.org/10.5194/amt-10-549-2017, 2017.

      Etheridge, D., Gregory, R., Allison, C., Kuske, T., Berko, H., Schroder, I., Loh, Z., Feitz, A. J., Hibberd, M., Zegelin, S., et al.: Metadata
        report: Arcturus atmospheric greenhouse gas monitoring, Geoscience Australia, 2014.

      Etheridge, D., Day, S., Hibberd, M., Luhar, A., Spencer, D., Loh, Z., Zegelin, S., Krummel, P., van Gorsel, E., Thornton, D., et al.: Charac-
535   terisation of Regional Fluxes of Methane in the Surat Basin, Queensland, 2016.

      FIRM: The Fire Information for Resource Management System (FIRMS), https://firms.modaps.eosdis.nasa.gov/map/
        ,lastaccessed2020-07-18, 2020.

      Friedlingstein, P., Jones, M. W., O'Sullivan, M., Andrew, R. M., Hauck, J., Peters, G. P., Peters, W., Pongratz, J., Sitch, S., Le Quéré, C.,
        Bakker, D. C. E., Canadell, J. G., Ciais, P., Jackson, R. B., Anthoni, P., Barbero, L., Bastos, A., Bastrikov, V., Becker, M., Bopp, L.,
540   Buitenhuis, E., Chandra, N., Chevallier, F., Chini, L. P., Currie, K. I., Feely, R. A., Gehlen, M., Gilfillan, D., Gkritzalis, T., Goll, D. S.,
        Gruber, N., Gutekunst, S., Harris, I., Haverd, V., Houghton, R. A., Hurtt, G., Ilyina, T., Jain, A. K., Joetzjer, E., Kaplan, J. O., Kato, E.,
        Klein Goldewijk, K., Korsbakken, J. I., Landschützer, P., Lauvset, S. K., Lefèvre, N., Lenton, A., Lienert, S., Lombardozzi, D., Marland,
        G., McGuire, P. C., Melton, J. R., Metzl, N., Munro, D. R., Nabel, J. E. M. S., Nakaoka, S.-I., Neill, C., Omar, A. M., Ono, T., Peregon,
        A., Pierrot, D., Poulter, B., Rehder, G., Resplandy, L., Robertson, E., Rödenbeck, C., Séférian, R., Schwinger, J., Smith, N., Tans, P. P.,
545   Tian, H., Tilbrook, B., Tubiello, F. N., van der Werf, G. R., Wiltshire, A. J., and Zaehle, S.: Global Carbon Budget 2019, Earth System
        Science Data, 11, 1783–1838, https://doi.org/10.5194/essd-11-1783-2019, https://essd.copernicus.org/articles/11/1783/2019/, 2019.

      Grell, G. A. and Dévényi, D.: A generalized approach to parameterizing convection combining ensemble and data assimilation techniques,
        Geophysical Research Letters, 29, 38–1–38–4, https://doi.org/10.1029/2002GL015311, http://doi.wiley.com/10.1029/2002GL015311,
        2002.

550   Griffith, D., Deutscher, N., Velazco, V., Wennberg, P., Yavin, Y., Aleks, G. K., Washenfelder, R., Toon, G., Blavier, J., Murphy, C., et al.:
        TCCON data from Darwin, Australia, Release GGG2014R0, TCCON data archive, hosted by Caltech-DATA, California Institute of
        Technology, Pasadena, CA, USA, https://doi.org/http://doi.org/10.14291/tccon.ggg2014.darwin01.R0/1149290, 2014a.

Griffith, D., Velazco, V., Deutscher, N., Murphy, C., Jones, N., Wilson, S., Macatangay, R., Kettlewell, G., Buchholz, R., and Riggenbach, M.: TCCON data from Wollongong, Australia, Release GGG2014R0. TCCON data archive, hosted by CaltechDATA, California Institute
555   of Technology, Pasadena, CA, U.S.A, https://doi.org/https://doi.org/10.14291/tccon.ggg2014.wollongong01.R0/1149291, 2014b.

Hakami, A., Henze, D. K., Seinfeld, J. H., Singh, K., Sandu, A., Kim, S., Byun, and Li, Q.: The Adjoint of CMAQ, Environmental Science
     & Technology, 41, 7807–7817, https://doi.org/10.1021/es070944p, https://doi.org/10.1021/es070944p, pMID: 18075092, 2007.

Harverd, V.: personal communication, 2020.

Haverd, V., Raupach, M. R., Briggs, P. R., Canadell., J. G., Davis, S. J., Law, R. M., Meyer, C. P., Peters, G. P., Pickett-Heaps, C., and
560   Sherman, B.: The Australian terrestrial carbon budget, Biogeosciences, 10, 851–869, https://doi.org/10.5194/bg-10-851-2013, 2013a.

Haverd, V., Raupach, M. R., Briggs, P. R., Canadell, J. G., Isaac, P., Pickett-Heaps, C., Roxburgh, S. H., van Gorsel, E., Viscarra Rossel,
     R. A., and Wang, Z.: Multiple observation types reduce uncertainty in Australia's terrestrial carbon and water cycles, Biogeosciences, 10,
     2011–2040, https://doi.org/10.5194/bg-10-2011-2013, https://bg.copernicus.org/articles/10/2011/2013/, 2013b.

Haverd, V., Smith, B., Cook, G. D., Briggs, P. R., Nieradzik, L., Roxburgh, S. H., Liedloff, A., Meyer, C. P., and Canadell, J. G.: A
565   stand-alone tree demography and landscape structure module for Earth system models, Geophysical Research Letters, 40, 5234–5239,
     https://doi.org/https://doi.org/10.1002/grl.50972, https://agupubs.onlinelibrary.wiley.com/doi/abs/10.1002/grl.50972, 2013c.

Haverd, V., Raupach, M. R., Briggs, P. R., Canadell, J. G., Davis, S. J., Law, R. M., Meyer, C. P., Peters, G. P., Pickett-Heaps, C., and Sherman,
     B.: Corrigendum to "The Australian Terrestrial Carbon Budget" published in Biogeosciences, 10, 851–869, 2013, Biogeosciences, 12,
     3603–3605, https://doi.org/10.5194/bg-12-3603-2015, http://www.biogeosciences.net/12/3603/2015/, 2015.

570 Haverd, V., Smith, B., Nieradzik, L., Briggs, P. R., Woodgate, W., Trudinger, C. M., Canadell, J. G., and Cuntz, M.: A new version of the
     CABLE land surface model (Subversion revision r4601) incorporating land use and land cover change, woody vegetation demography,
     and a novel optimisation-based approach to plant coordination of photosynthesis, Geoscientific Model Development, 11, 2995–3026,
     https://doi.org/10.5194/gmd-11-2995-2018, https://gmd.copernicus.org/articles/11/2995/2018/, 2018.

Iacono, M. J., Delamere, J. S., Mlawer, E. J., Shephard, M. W., Clough, S. A., and Collins, W. D.: Radiative forcing by long-
575   lived greenhouse gases: Calculations with the AER radiative transfer models, Journal of Geophysical Research, 113, D13 103,
     https://doi.org/10.1029/2008JD009944, http://doi.wiley.com/10.1029/2008JD009944, 2008.

Janjić, Z. I.: The Step-Mountain Eta Coordinate Model: Further Developments of the Convection, Viscous Sublayer, and Turbulence Closure
     Schemes, Monthly Weather Review, 122, 927–945, https://doi.org/10.1175/1520-0493(1994)122<0927:TSMECM>2.0.CO;2, 1994.

Jones, D. A., Wang, W., and Fawcett, R.: High-quality spatial climate data-sets for Australia, Australian Meteorological and Oceanographic
580   Journal, 58, 233, 2009.

Kaminski, T., Rayner, P. J., Heimann, M., and Enting, I. G.: On aggregation errors in atmospheric transport inversions, Journal of Geophysical
     Research, 106, 4703, https://doi.org/10.1029/2000JD900581, 2001.

Kawasaki, M., Yoshioka, H., Jones, N. B., Macatangay, R., Griffith, D. W. T., Kawakami, S., Ohyama, H., Tanaka, T., Morino, I., Uchino,
     O., and Ibuki, T.: Usability of optical spectrum analyzer in measuring atmospheric CO_2 and CH_4 column densities: inspection with
585   FTS and aircraft profiles in situ, Atmospheric Measurement Techniques, 5, 2593–2600, https://doi.org/10.5194/amt-5-2593-2012, https:
     //amt.copernicus.org/articles/5/2593/2012/, 2012.

Kiel, M., O'Dell, C. W., Fisher, B., Eldering, A., Nassar, R., MacDonald, C. G., and Wennberg, P. O.: How bias correction goes wrong:
     measurement of XCO2 affected by erroneous surface pressure estimates., Atmospheric Measurement Techniques, 12, 2019.

Krinner, G., Viovy, N., de Noblet-Ducoudré, N., Ogée, J., Polcher, J., Friedlingstein, P., Ciais, P., Sitch, S., and Prentice, I. C.: A dy-
namic global vegetation model for studies of the coupled atmosphere-biosphere system, Global Biogeochemical Cycles, 19, 1–33,
https://doi.org/10.1029/2003GB002199, 2005.

Lafayette, L., Sauter, G., Vu, L., and Meade, B.: "Spartan Performance and Flexibility: An HPC-Cloud Chimera", OpenStack Summit,
Barcelona, October, https://doi.org/https://doi.org/10.4225/49/58ead90dceaaa, 2016.

Law, R. M., Rayner, P. J., and Wang, Y. P.: Inversion of diurnally varying synthetic CO_2: Network optimization for an Australian
test case, Global Biogeochemical Cycles, 18, https://doi.org/10.1029/2003GB002136, https://agupubs.onlinelibrary.wiley.com/doi/abs/
10.1029/2003GB002136, 2004.

Le Quéré, C., Andrew, R. M., Friedlingstein, P., Sitch, S., Hauck, J., Pongratz, J., Pickers, P. A., Korsbakken, J. I., Peters, G. P., Canadell,
J. G., Arneth, A., Arora, V. K., Barbero, L., Bastos, A., Bopp, L., Chevallier, F., Chini, L. P., Ciais, P., Doney, S. C., Gkritzalis, T., Goll,
D. S., Harris, I., Haverd, V., Hoffman, F. M., Hoppema, M., Houghton, R. A., Hurtt, G., Ilyina, T., Jain, A. K., Johannessen, T., Jones,
C. D., Kato, E., Keeling, R. F., Goldewijk, K. K., Landschützer, P., Lefèvre, N., Lienert, S., Liu, Z., Lombardozzi, D., Metzl, N., Munro,
D. R., Nabel, J. E. M. S., Nakaoka, S., Neill, C., Olsen, A., Ono, T., Patra, P., Peregon, A., Peters, W., Peylin, P., Pfeil, B., Pierrot, D.,
Poulter, B., Rehder, G., Resplandy, L., Robertson, E., Rocher, M., Rödenbeck, C., Schuster, U., Schwinger, J., Séférian, R., Skjelvan,
I., Steinhoff, T., Sutton, A., Tans, P. P., Tian, H., Tilbrook, B., Tubiello, F. N., van der Laan-Luijkx, I. T., van der Werf, G. R., Viovy,
N., Walker, A. P., Wiltshire, A. J., Wright, R., Zaehle, S., and Zheng, B.: Global Carbon Budget 2018, Earth System Science Data, 10,
2141–2194, https://doi.org/10.5194/essd-10-2141-2018, https://essd.copernicus.org/articles/10/2141/2018/, 2018.

Loh, Z.: personal communication, 2019.

Ma, X., Huete, A., Cleverly, J., Eamus, D., Chevallier, F., Joiner, J., Poulter, B., Zhang, Y., Guanter, L., Meyer, W., Xie, Z., and Ponce-
Campos, G.: Drought rapidly diminishes the large net CO2 uptake in 2011 over semi-arid Australia, Scientific Reports, 6, 37 747,
https://doi.org/10.1038/srep37747, http://www.nature.com/articles/srep37747, 2016.

Maksyutov, S., Takagi, H., Valsala, V. K., Saito, M., Oda, T., Saeki, T., Belikov, D. A., Saito, R., Ito, A., Yoshida, Y., Morino, I., Uchino,
O., Andres, R. J., and Yokota, T.: Regional CO_2 flux estimates for 2009–2010 based on GOSAT and ground-based CO2 observations,
Atmospheric Chemistry and Physics, 13, 9351–9373, https://doi.org/10.5194/acp-13-9351-2013, http://www.atmos-chem-phys.net/13/
9351/2013/, 2013.

Michalak, A. M., Hirsch, A., Bruhwiler, L., Gurney, K. R., Peters, W., and Tans, P. P.: Maximum likelihood estimation of covariance
parameters for Bayesian atmospheric trace gas surface flux inversions, Journal of Geophysical Research Atmospheres, 110, 1–16,
https://doi.org/10.1029/2005JD005970, 2005.

Monin, A. S. and Obukhov, A.: Basic laws of turbulent mixing in the surface layer of the atmosphere., Contrib. Geophys. Inst. Acad. Sci.
USSR, 151, 163–187, monin1954, 1954.

Morgan, J., Fensham, R., Godfree, R., and Foreman, P.: Australian tussock grasslands, Australian Vegetation, p. 438, 2017.

Morrison, H., Thompson, G., and Tatarskii, V.: Impact of Cloud Microphysics on the Development of Trailing Stratiform Precip-
itation in a Simulated Squall Line: Comparison of One-and Two-Moment Schemes, Monthly Weather Review, 137, 991–1007,
https://doi.org/10.1175/2008MWR2556.1, http://journals.ametsoc.org/doi/abs/10.1175/2008MWR2556.1, 2009.

Nassar, R., Napier-Linton, L., Gurney, K. R., Andres, R. J., Oda, T., Vogel, F. R., and Deng, F.: Improving the temporal and spatial dis-
tribution of CO2 emissions from global fossil fuel emission data sets, Journal of Geophysical Research: Atmospheres, 118, 917–933,
https://doi.org/10.1029/2012JD018196, https://agupubs.onlinelibrary.wiley.com/doi/abs/10.1029/2012JD018196, 2013.

OCO-2 Science Team/Michael Gunson, Annmarie Eldering: OCO-2 Level 2 bias-corrected XCO2 and other select fields from the full-physics retrieval aggregated as daily files, Retrospective processing V9r, Greenbelt, MD, USA, Goddard Earth Sciences Data and Information Services Center (GES DISC), https://doi.org/10.5067/W8QGIYNKS3JC, https://disc.gsfc.nasa.gov/datacollection/OCO2_L2_Lite_FP_9r.html, 2018.

630 Oda, T., Maksyutov, S., and Andres, R. J.: The Open-source Data Inventory for Anthropogenic CO_2, version 2016 (ODIAC2016): a global monthly fossil fuel CO_2 gridded emissions data product for tracer transport simulations and surface flux inversions, Earth System Science Data, 10, 87–107, https://doi.org/10.5194/essd-10-87-2018, https://essd.copernicus.org/articles/10/87/2018/, 2018.

Otte, T. L. and Pleim, J. E.: The Meteorology-Chemistry Interface Processor (MCIP) for the CMAQ modeling system: updates through MCIPv3.4.1, Geoscientific Model Development, 3, 243–256, https://doi.org/10.5194/gmd-3-243-2010, http://www.geosci-model-dev.net/635 3/243/2010/, 2010.

Patra, P. K., Takigawa, M., Watanabe, S., Chandra, N., Ishijima, K., and Yamashita, Y.: Improved Chemical Tracer Simulation by MIROC4.0-based Atmospheric Chemistry-Transport Model (MIROC4-ACTM), SOLA, 14, 91–96, https://doi.org/10.2151/sola.2018-016, 2018.

Poulter, B., Frank, D., Ciais, P., Myneni, R. B., Andela, N., Bi, J., Broquet, G., Canadell, J. G., Chevallier, F., Liu, Y. Y., Running, S. W., Sitch, S., and van der Werf, G. R.: Contribution of semi-arid ecosystems to interannual variability of the global carbon cycle, Nature, 509, 640 600–603, https://doi.org/10.1038/nature13376, http://www.nature.com/doifinder/10.1038/nature13376, 2014.

Rayner, P. J., Enting, I. G., Francey, R. J., and Langenfelds, R.: Reconstructing the recent carbon cycle from atmospheric CO_2, $\delta^{13}C$ and O_2/N_2 observations*, Tellus B, 51, 213–232, https://doi.org/https://doi.org/10.1034/j.1600-0889.1999.t01-1-00008.x, 1999.

Rayner, P. J., Michalak, A. M., and Chevallier, F.: Fundamentals of data assimilation applied to biogeochemistry, Atmospheric Chemistry and Physics, 19, 13 911–13 932, https://doi.org/10.5194/acp-19-13911-2019, https://www.atmos-chem-phys.net/19/13911/2019/, 2019.

645 Rödenbeck, C., Houweling, S., Gloor, M., and Heimann, M.: CO_2 flux history $1982 - 2001$ inferred from atmospheric data using a global inversion of atmospheric transport, Atmospheric Chemistry and Physics, 3, 1919–1964, https://doi.org/10.5194/acp-3-1919-2003, https://acp.copernicus.org/articles/3/1919/2003/, 2003.

Running, S., Mu, Q., and Zhao, M.: MOD17A2H MODIS/terra gross primary productivity 8-day L4 global 500m SIN grid V006, https://lpdaac.usgs.gov/products/mod17a2hv006,lastaccessed2019-09-10, 2015.

650 Schuh, A. E., Denning, A. S., Corbin, K. D., Baker, I. T., Uliasz, M., Parazoo, N., Andrews, A. E., and Worthy, D. E. J.: A regional high-resolution carbon flux inversion of North America for 2004, Biogeosciences, 7, 1625–1644, https://doi.org/10.5194/bg-7-1625-2010, http://www.biogeosciences.net/7/1625/2010/, 2010.

Sherlock, V., Connor, B., Robinson, J., Shiona, H., Smale, D., and Pollard, D.: TCCON data from Lauder, New Zealand, 125HR, Release GGG2014R0. TCCON data archive, hosted by CaltechDATA, California Institute of Technology, Pasadena, CA, U.S.A., 655 https://doi.org/https://doi.org/10.14291/tccon.ggg2014.lauder02.R0/1149298, 2014.

Sitch, S., Friedlingstein, P., Gruber, N., Jones, S. D., Murray-Tortarolo, G., Ahlström, A., Doney, S. C., Graven, H., Heinze, C., Huntingford, C., Levis, S., Levy, P. E., Lomas, M., Poulter, B., Viovy, N., Zaehle, S., Zeng, N., Arneth, A., Bonan, G., Bopp, L., Canadell, J. G., Chevallier, F., Ciais, P., Ellis, R., Gloor, M., Peylin, P., Piao, S. L., Le Quéré, C., Smith, B., Zhu, Z., and Myneni, R.: Recent trends and drivers of regional sources and sinks of carbon dioxide, Biogeosciences, 12, 653–679, https://doi.org/10.5194/bg-12-653-2015, http://660 //www.biogeosciences.net/12/653/2015/, 2015.

Skamarock, W., Klemp, J., Dudhi, J., Gill, D., Barker, D., Duda, M., Huang, X.-Y., Wang, W., and Powers, J.: A Description of the Advanced Research WRF Version 3, Technical Report, p. 113, https://doi.org/10.5065/D6DZ069T, 2008.

Tarantola, A.: Inverse Problem Theory: methods for data fitting and model parameter estimation, Elsevier, 1987.

Tewari, M., Chen, F., Kusaka, H., and Miao, S.: Coupled WRF/Unified Noah/Urban-Canopy Modeling System, NCAR WRF Documentation, pp. 1–20, https://ral.ucar.edu/sites/default/files/public/product-tool/WRF-LSM-Urban.pdf, 2007.

Thomas, S.: Bayesian variational assimilation code py4dvar, https://github.com/steven-thomas/py4dvar, 2020.

Trudinger, C. M., Haverd, V., Briggs, P. R., and Canadell, J. G.: Interannual variability in Australia's terrestrial carbon cycle constrained by multiple observation types, Biogeosciences, 13, 6363–6383, https://doi.org/10.5194/bg-13-6363-2016, 2016.

van der Laan-Luijkx, I. T., van der Velde, I. R., van der Veen, E., Tsuruta, A., Stanislawska, K., Babenhauserheide, A., Zhang, H. F., Liu, Y., He, W., Chen, H., Masarie, K. A., Krol, M. C., and Peters, W.: The CarbonTracker Data Assimilation Shell (CTDAS) v1.0: implementation and global carbon balance 2001–2015, Geoscientific Model Development, 10, 2785–2800, https://doi.org/10.5194/gmd-10-2785-2017, https://gmd.copernicus.org/articles/10/2785/2017/, 2017.

van der Werf, G. R., Randerson, J. T., Giglio, L., van Leeuwen, T. T., Chen, Y., Rogers, B. M., Mu, M., van Marle, M. J. E., Morton, D. C., Collatz, G. J., Yokelson, R. J., and Kasibhatla, P. S.: Global fire emissions estimates during 1997–2016, Earth System Science Data, 9, 697–720, https://doi.org/10.5194/essd-9-697-2017, https://www.earth-syst-sci-data.net/9/697/2017/, 2017.

Villalobos, Y., Rayner, P., Thomas, S., and Silver, J.: The potential of Orbiting Carbon Observatory-2 data to reduce the uncertainties in CO_2 surface fluxes over Australia using a variational assimilation scheme, Atmospheric Chemistry and Physics, 20, 8473–8500, https://doi.org/10.5194/acp-20-8473-2020, https://www.atmos-chem-phys.net/20/8473/2020/, 2020.

Wang, J., Li, A., and Bian, J.: Simulation of the grazing effects on grassland aboveground net primary production using DNDC model combined with time-series remote sensing data—a case study in Zoige Plateau, China, Remote Sensing, 8, 168, 2016.

Wang, Y. P., Law, R. M., and Pak, B.: A global model of carbon, nitrogen and phosphorus cycles for the terrestrial biosphere, Biogeosciences, 7, 2261–2282, https://doi.org/10.5194/bg-7-2261-2010, https://bg.copernicus.org/articles/7/2261/2010/, 2010.

Weltzin, J. F., Loik, M. E., Schwinning, S., Williams, D. G., Fay, P. A., Haddad, B. M., Harte, J., Huxman, T. E., Knapp, A. K., Lin, G., Pockman, W. T., Shaw, R. M., Small, E. E., Smith, M. D., Smith, S. D., Tissue, D. T., and Zak, J. C.: Assessing the Response of Terrestrial Ecosystems to Potential Changes in Precipitation, BioScience, 53, 941–952, https://doi.org/10.1641/0006-3568(2003)053[0941:ATROTE]2.0.CO;2, https://doi.org/10.1641/0006-3568(2003)053[0941:ATROTE]2.0.CO;2, 2003.

Wunch, D., Toon, G. C., Blavier, J.-F. L., Washenfelder, R. A., Notholt, J., Connor, B. J., Griffith, D. W. T., Sherlock, V., and Wennberg, P. O.: The Total Carbon Column Observing Network, Philosophical Transactions of the Royal Society A: Mathematical, Physical and Engineering Sciences, 369, 2087–2112, https://doi.org/10.1098/rsta.2010.0240, http://rsta.royalsocietypublishing.org/cgi/doi/10.1098/rsta.2010.0240, 2011.

Yokota, T., Yoshida, Y., Eguchi, N., Ota, Y., Tanaka, T., Watanabe, H., and Maksyutov, S.: Global Concentrations of CO_2 and CH_4 Retrieved from GOSAT: First Preliminary Results, SOLA, 5, 160–163, https://doi.org/10.2151/sola.2009-041, 2009.

Zhao, C. L. and Tans, P. P.: Estimating uncertainty of the WMO mole fraction scale for carbon dioxide in air, Journal of Geophysical Research: Atmospheres, 111, https://doi.org/https://doi.org/10.1029/2005JD006003, https://agupubs.onlinelibrary.wiley.com/doi/abs/10.1029/2005JD006003, 2006.